Identification of Druggable Binding Sites and Small Molecules as Modulators of TMC1

Pedro De-la-Torre[1,*,†], Claudia Martínez-García[2,†], Paul Gratias[1,†], Matthew Mun[1], Paula Santana[3], Nurunisa Akyuz[4], Wendy González[5], Artur A. Indzhykulian[1,*], David Ramírez[2,*].

Affiliations:

[1]Department of Otolaryngology - Head and Neck Surgery, Harvard Medical School and Mass Eye and Ear, Boston, MA, USA

[2]Department of Pharmacology, Faculty of Biological Sciences, University of Concepción, Chile.

[3]Facultad de Ingeniería, Instituto de Ciencias Químicas Aplicadas, Universidad Autónoma de Chile, Santiago, Chile

[4]Department of Neurobiology, Harvard Medical School, Boston, MA, USA

[5]Center for Bioinformatics and Molecular Simulations (CBSM), University of Talca, Talca 3460000, Chile

[*]Correspondence should be addressed to:

dramirezs@udec.cl,

inartur@hms.harvard.edu,

pedro_delatorremarquez@meei.harvard.edu

[†]These authors contributed equally to this work

Abstract

Our ability to hear and maintain balance relies on the proper functioning of inner ear sensory hair cells, which translate mechanical stimuli into electrical signals via mechano-electrical transducer (MET) channels, composed of TMC1/2 proteins. However, the therapeutic use of ototoxic drugs, such as aminoglycosides and cisplatin, which can enter hair cells through MET channels, often leads to profound auditory and vestibular dysfunction. Despite extensive research on otoprotective compounds targeting MET channels, our understanding of how small molecule modulators interact with these channels remains limited, hampering the discovery of novel compounds. Here, we propose a structure-based screening approach, integrating 3D-pharmacophore modeling, molecular simulations, and experimental validation. Our pipeline successfully identified several novel compounds and FDA-approved drugs that reduced dye uptake in cultured cochlear explants, indicating MET modulation activity. Molecular docking and free-energy estimations for binding allowed us to identify three potential drug binding sites within the channel pore, phospholipids, and key amino acids involved in modulator interactions. We also identified shared ligand-binding features between TMC and structurally related TMEM16 protein families, providing novel insights into their distinct inhibition, while potentially guiding the rational design of MET-channel-specific modulators. Our pipeline offers a broad application to discover small molecule modulators for a wide spectrum of mechanosensitive ion channels.

Introduction

The sensory hair cells of the inner ear function as mechanoreceptors, converting various mechanical stimuli—including sound-induced vibrations, gravitational forces, and linear acceleration—into electrical signals, mediating our senses of hearing and balance. However, deficiencies or malfunctions in hair cells, stemming from genetic mutations[1,2], aging[3], exposure to loud noise[4], or drug-induced ototoxicity, often result in hearing loss. Notably, platinum-containing chemotherapeutic drugs[5,6] and the aminoglycoside (AG) group of antibiotics are known ototoxic agents that cause hearing loss and balance dysfunction[5,7].

Furthermore, recent studies suggest that non-AG antibiotics may also cause ototoxicity, although clinical reports of such cases are less frequent[8]. AG ototoxicity may occur due to several factors, including the administration of doses exceeding the therapeutic range, or the use of enantiomeric mixtures of AG[9]. Several mechanisms have been implicated in AG-induced hearing loss[10–15]. It is widely recognized that AG uptake into hair cells primarily occurs through the mechanoelectrical transduction (MET) channels formed by the pore-forming TMC1/2 proteins[16–20]. Surprisingly, about 9000 dihydrostreptomycin (DHS) molecules per second are predicted to enter into hair cells in a voltage-dependent manner[21], at therapeutic concentrations[17].

The MET channels are gated by force transmitted through tip-link filaments[22,23] composed of cadherin-23 (CDH23)[24,25] and protocadherin-15 (PCDH15)[26–30]. The resting tension applied by the tip link to the MET channel complex results in an increased open probability of MET channels at rest, enabling AG uptake[30,31]. Consequently, disruption of tip links by calcium (Ca^{2+}) chelators closes the MET channel, preventing AG uptake into hair cells[20]. These findings inspired numerous studies aimed at identifying MET channel blockers for use as otoprotective compounds, predating the identification of molecules that form the MET channel complex[19,32–37]. The identification of TMC1 as the pore-forming channel subunit has opened up new venues of research for identifying novel pharmacological agents capable of reversibly blocking the MET channel.

Similar to AG treatment, cisplatin causes permanent hearing loss in a significant percentage of treated patients, due to its gradual accumulation in the cochlea over months to years[38]. Given the impact caused by ototoxic side effects of both AG and cisplatin, the pursuit for novel drugs to prevent the resulting hearing loss is ongoing[32–34,39–41]. Currently, there are at least 17 clinical trials evaluating 10 different therapeutics to prevent aminoglycoside and/or cisplatin-induced ototoxicity[42]. Recently, the Food and Drug Administration (FDA) approved sodium thiosulfate (STS) to reduce the risk of cisplatin-induced ototoxicity in pediatric patients[43,44], although its mechanism of action is not fully understood[45]. Studies using animal models, however, suggest that STS does not protect hair cells against AG-induced cell death[46], and it remains unclear whether STS interacts with the MET channel[47–51]. This underscores the need for structure-guided search for novel otoprotectants to mitigate ototoxicity mediated by the MET channel in order to prevent hearing loss in children and adults.

Multiple studies have focused on designing or structurally modifying small molecules to serve as potential otoprotectants against AG-induced hair-cell loss[19,32–35,41,52,53]. However, their interactions within the TMC1 pore remain largely unknown, and whether these compounds share any common TMC1-binding mechanisms is not well understood[17,18,54–58]. Previously reported molecule screen using a chemical library of 10,240 compounds, identified UoS-7692 and several others as potent MET blocker[32] (**Figure 1**). This compound demonstrated strong otoprotection against AG in zebrafish larval hair cells and in mouse cochlear explants[32].

While experimental screening of relatively small libraries of compounds typically focuses on their *in vitro* and *in vivo* evaluation in hair cell-like cell lines, live zebrafish larvae or in mouse cochlear explants, this laborious and a relatively low-throughput approach limits exploration of the broad chemical space. Interestingly, no *in silico* data evaluating binding modes of known MET channel blockers within the TMC1 pore cavity has been reported to date. Therefore, conducting an *in silico* screen to evaluate the binding of potential MET channel blockers to TMC1, followed by more conventional *in vitro* experiments to confirm the *in silico* predictions, is an attractive strategy for discovering novel TMC1 modulators.

The pharmacophore concept, defined as the set of structural features recognized at a receptor site or derived from the structure of a ligand, plays a crucial role in determining the bioactivity of a molecule[59,60], and serves as a valuable tool in drug discovery. However, the application of a ligand-base pharmacophore concept for discovering novel TMC1 modulators remains largely unexplored in the context of drug discovery, and the 3D-pharmacophoric and structural factors involved in TMC1-ligand interactions are not well understood. Given the structural diversity of compounds reported as potential MET channel blockers[19,32–37,53] (**Figure 1**), conducting a comprehensive study to analyze their shared ligand-based pharmacophoric features and their binding to TMC1 is essential to identifying or developing potent and selective MET channel modulators that could potentially serve as otoprotectants. Conversely, considering that TMC1 proteins share structural and sequence similarities with the TMEM16 and OSCA families of membrane proteins[18,54,61–64], potential ligand-based pharmacophores from molecules that modulate their function could also be employed to explore the polypharmacology of these related proteins.

In silico pharmacophore modeling[65–68], molecular docking[69–76], and binding free energy[77–79] studies have emerged as powerful methods for discovering bioactive small molecules. These methods enable a deeper understanding of the key structural factors and moieties required for hit-to-lead optimization with improved biological activities. Previously, we have successfully utilized these methods to design blockers for several ion channels as well as to design other small molecules of biological relevance[80–83].

In this study, we devised a versatile computational strategy to explore the binding modes of known TMC1 blockers and to identify novel modulators of TMC1. Our strategy combines *in silico* modeling with experimental validation of compounds in mouse cochlear explants. First, we developed common 3D-ligand-based pharmacophore models for small molecules based on known MET channel blockers and predicted their binding modes within the TMC1 druggable pore. These models enabled us to pre-select 258 candidate compounds from over ~22 million compounds (representing ~220 million conformers), sourced from two distinct chemical libraries (non-FDA-approved and FDA-approved drugs).

Subsequently, we utilized AlphaFold2-based structural predictions of the TMC1 protein in an open-like state[84] to carry out virtual screening (VS) of these 258 molecules, to predict their potential binding modes. Furthermore, we conducted a comparison of the 3D-pharmacophore features exhibited by TMC1 blockers with those of compounds reported to modulate the activity of the paralog TMEM16A protein, to identify potential structure-pharmacophoric relationships.

After conducting virtual screening, we further assessed the binding energies of the docking poses by predicting their binding-free energies using molecular mechanics with generalized Born and surface area (MM/GBSA) methods. From each library, we selected the top 10 hits based on their predicted binding energies and structural diversity for subsequent *in vitro* evaluation, ensuring their commercial availability for experimental testing. Next, the MET blocking capacity of each hit candidate was evaluated *in vitro* using the AM1-43[55] dye uptake assay in mouse cochlear explants using live microscopy imaging. AM1-43, developed as a fixable analogue of FM1-43, functions effectively in live tissue along with FM1-43. Our screening pipeline successfully identified hit compounds that demonstrated a reduction of AM1-43 uptake in cochlear hair cells. A schematic of the pipeline is presented in **Scheme 1**.

In summary, we have developed and experimentally validated, for the first time, a set of effective 3D-pharmacophore models and successfully utilized them to identify novel families of MET channel modulators. We then predicted the binding of these compounds within the pore of the TMC1 channel and provide a list of potential binding sites for both known and newly discovered modulators within the pore. This structural modeling approach, combined with experimental evaluation in hair cells, allowed us to reveal new putative binding sites critical for ligand interaction within the TMC1 pore, as well as potential shared pharmacophoric properties between small molecules reported to interact with both TMC1 and TMEM16A proteins[85].

Results

Building a good-quality structural model of TMC1 for virtual screening

Homology and experimental structural models for TMC1 and TMC2 have contributed to identifying a putative pore and providing insights into the ion permeation pathway[18,63,84,86]. Cryo-electron microscopy (Cryo-EM) structures of *C. elegans* (*Ce*) TMC1 have confirmed at the atomic level the structural similarities between TMCs and TMEM16, and TMEM63/OSCA protein families[54,61,63,87]. Specifically, TMC1 assembles as dimers with 10 transmembrane (TM) domains in each subunit, similar to TMEM16 proteins[63], or OSCA channels which have 11 TM domains[64].

In the absence of 3D-atomic structures of the mammalian MET-channel complex, we constructed a model of the complex by assembling *Mus musculus* (*Mm*) TMC1 subunits with *Mm*CIB2 and *Mm*TMIE. *Mm*CIB2 was included to increase the stability of the MET complex and preserve its influence in phospholipid dynamics and ion permeation[88,89]. We utilized the Cryo-EM structure of the expanded *Ce*TMC-1 complex (PDB code: 7USW)[54] as a reference for structural alignment, and employed the Maestro software for structural modeling. The assembled complex was compared with the cryo-EM structure of the expanded *Ce*TMC-1 complex, confirming that the TM10 domain was in the typical domain-swapped conformation[54], which is a structural requirement for the proper oligomerization of *mm*TMC1 (**Figure 2**).

Next, the model was subjected to energy minimization, followed by embedding into a pre-equilibrated 1-palmitoyl-2-oleoyl-sn-glycero-3-phosphocholine (POPC) phospholipid membrane and solvation with a final ionic concentration of 15 mM KCl (**Figure 2**) (See *Methods*). Subsequently, the system underwent 25 ns of restrained equilibrium molecular dynamics simulation (MDs). The Root Mean Square Deviation (RMSD), which measures global structural changes across all backbone atoms in the model, was monitored (**Figure 2F**) to evaluate conformational stability. Equilibration was achieved after 2 ns of MDs, and the RMSD of all backbone atoms remained within 2Å distance for the entire complex (**Supp Figure 1A**), indicating stable conformation of the modeled structure.

When analyzing hetero-subunits independently, both TMC1 and CIB2 protomers remained stable during the 25 ns MDs, with RMSD values at ~2Å. However, fluctuations were observed in the C-terminal TMIE domain, with RMSD values within 4Å along the trajectory. This behavior was likely attributable to a kinked-flexible linker between its transmembrane and cytoplasmic domains, allowing for the cytoplasmic fragment to move more freely (**Figure 2C**, and **Supp Figure 1A**).

Root Mean Square Fluctuation (RMSF) analysis, which assesses local atomic fluctuations and flexibility, revealed that TMC1 chains exhibited fluctuations under 2Å, except for specific loop regions between residues (**Supp Figure 1C**). Even though TMIE has limited interactions with TMC1, its N-terminal TM domain fragment presented low fluctuations, likely because it is embedded within the bilayer membrane (**Figure 2C**, and **Supp Figure 1C**). In contrast, the TMIE C-terminal fragment displayed larger fluctuations mostly because it is positioned outside the bilayer membrane and is exposed to solvent, hinging about a flexible region (**Figure 2C** and, see **Supp Figure 1C**). Like TMIE, the CIB2 protomers displayed similar RMSF fluctuations within its N-terminal domains, likely due to the random-coil configuration of these regions (**Supp Figure 1C**). The distribution of atoms within the MET complex was assessed using the radius of gyration measurements (**Supp Figure 1C**), and no major changes were detected, with the radius of gyration remaining within 1Å.

During the 25 ns MD simulations, various phospholipids were observed to migrate into the pore, positioning their polar heads near the top and the bottom of the putative TMC1 pore cavity, with their hydrophobic tails directed towards the pore (**Figure 2F**, and **Figure 5C, 5G-I**). Such lipid movements along the trajectory agrees with the findings reported in the literature[54,89], where phospholipids were suggested to move dynamically between the TM4 and TM6 domains of TMC1[88,89], providing further insights into the structural dynamics and lipid-protein interactions within the TMC1 pore.

Furthermore, our analysis revealed the presence of several water molecules and potassium (K^+) ions within the pore cavity during the MD simulation, indicating the existence of a hydrated pore (**Figure 2F**). These findings are in agreement with previous reports, highlighting the significance of a hydrated environment in facilitating potential drug binding within the TMC1 pore[18,54,56,86,88,89], further supporting our structural model.

The combination of MD simulations and channel pore analysis by HOLE[90], has facilitated the identification of three primary target regions within the two elongated TMC1 pores (**Figure 2**). Along the *Z* axis, we have assigned these regions to an expanded top area located near the extracellular region, a narrowed middle area within the transmembrane segment, and a more expanded bottom area near the intracellular region (**Figure 2A**). The target regions we identified are suitable for screening of druggable-binding sites within the pore and can facilitate a comprehensive conformational search of both known and novel TMC1 interacting molecules using molecular docking (**Figure 1**, and **Figure 2B-E**).

Identification of common pharmacophores for MET channel block.

In this study, we analyzed the chemical structures of known MET channel blockers and identified 3D-pharmacophoric features that contribute to their antagonistic activity (**Figure 1, Table 1, Supp. Table 1**). These 3D elements may include specific functional groups, spatial arrangements, or physicochemical properties that are essential for binding to the MET channel and modulation of its function. The 3D-pharmacophoric models will then be used to screen large chemical databases to identify new candidate compounds with similar pharmacophoric features. Suitable hit compounds will be tested *in vitro*.

We used the software Phase[67] (See *Methods*) to design 3D pharmacophore models representing the main structural features of known MET channel blockers. These 3D-pharmacophore features were extracted by assembling a training set consisting of 13 structurally diverse compounds, which included UoS-7692[32], UoS-3607[32], UoS-3606[32], UoS-5247[32], UoS-962[32], Proto-1[91], E6-berbamine[53], hexamethyleneamiloride[36], amsacrine[36], phenoxybenzamine[36,92], carvedilol-derivate 13[52], ORC-13661[33,35], and FM1-43[57,58], a positively charged styryl dye often used to label hair cells and to check MET channel function[57,58] (**Figure 1** and **Supp. Table 1**).

These compounds coalesced to 10 predicted pharmacophores (**Table 1** and **Figure 3**), which were ranked based on PhaseHypoScore values[67]. The top-scoring pharmacophore, termed APRR (ID-1), achieved a PhaseHypoScore of 0.780. High PhaseHypoScore values indicate how well the pharmacophoric-feature vectors align with the structures of the compounds in the 3D-pharmacophore model (See *Methods*). All 10 3D-pharmacophores along with the matching compounds are reported in **Supp Table 2** and **Supp Figure 2**.

The APRR pharmacophore comprises four key features: one hydrogen bond acceptor group (A), one positively charged group (P), and two aromatic rings (R) (**Figure 3A**). Notably, this model matched 7 out of the 13 known MET blockers reported in the literature, which we used as a training set for this study (**Table 1, Figure 3A-I,** and **Supp. Table 2**). The remaining nine pharmacophores (ID #2 to #10) were modeled with three pharmacophoric features, reaching PhaseHypoScore values between 0.340 and 0.762 (**Table 1**).

Most of these pharmacophore models shared at least one common aromatic ring (R), and one acceptor group (A), except for the PRR (ID #4) and HPP (ID #10) models. Furthermore, the top four pharmacophores: APRR, APR-1, APR-3, and PRR (IDs #1 to #4) contained one protonatable group (P), matching 7 (APRR), 9 (APR-1), 8 (APR-3), and 7 (PRR) of the 13 known MET blockers, respectively. This suggests that a protonatable amine (positively charged N^+ group) is likely crucial for blocking TMC1 activity, consistent with experiments reported in the literature[32,52,56].

Pharmacophore-Based Virtual Screening of hit compounds.

Next, we employed Pharmacophore-Based Virtual Screening (PBVS), a method that involves computational screenning of large chemical databases to identify molecules that possess pharmacophoric features similar to a reference pharmacophore model[67]. In this study, we screened for compounds that matched any of the 10 pharmacophore models we developed. We used two libraries of compounds as databases; Library 1, boasting over 230 million commercially available, non-FDA-approved compounds (ZINC20 database)[93], and Library 2 (MicroSource Discovery Systems)[94] comprising 1,789 FDA-approved drugs.

PBVS was carried out using two consecutive steps. In the first step, we used ZINCPharmer[95], a free pharmacophore search software, to screen commercial compounds from the ZINC database[93]. The second

step involved using Phase (see *Methods*), which employs a PhaseScreenScore function that evaluates both the quantity (partial compound matching) and quality of ligand feature matching. This evaluation encompasses site, pharmacophore feature, and volume-scoring components for each compound[96].

The first step of our PBVS analysis commenced with the input of 10 pharmacophores into the ZINCPharmer[95] (see **Table 1** and **Supp. Figure 2**). We then selected the top 5,000 compounds with the lowest RMSD as a measurement of a good fit to the respective pharmacophore model, resulting in a total of 50,000 pre-filtered compounds (5,000 compounds × 10 pharmacophore models). After pharmacophore matching with ZINCPharmer, we selected only those compounds that matched with two or more pharmacophore models to increase the matching rate of our PBVS. This resulted in 4,187 compounds from the ZINC database that matched with two or more pharmacophore models (**Supp. Table 3**).

Next, the 4,187 chemical structures were processed using the LigPrep[97] and Epik[98,99] modules of the Maestro software[100] (See *Methods*) to structurally optimize the dataset and carry out the second step of PBVS with Phase. LigPrep module was used to generate 3D structures and optimize their geometry, while the Epik module was used for predicting up to 10 different optimized structures (i.e. conformations) per each of the 4,187 compounds, including their protonation and ionization states, tautomers, and chiralities at specific pH levels (see *Methods*). This increased the total number to 4,501 processed molecules, including 314 additional processed pair molecules, identified to be protonated or with a different structural conformation.

Subsequently, we carried out the second step of Phase-PBVS screening and calculated the highest PhaseScreenScore values from the 4,501 processed molecules corresponding to each of the 10 pharmacophore models. Of the 314 additional molecules that represented various confirmations of the original compounds, the best PhaseScreenScore value was selected across all conformations for the same compound, reducing the library down to 4,187 optimized molecules (Supp. Table 3).

The results were ranked based on their Total-PhaseScreenScore (TPS_S) ranging in values between 1.157 and 21.512, which were used to calculate the docking threshold (D_T, set to TPS_S score values above Mean + 2 SD), as a requirement to select the compounds for final molecular docking (see *Methods,* Equation 1) (**Figure 4A**). Of the 4,187 optimized compounds from Library 1, many aligned with several pharmacophore models (**Figure 4**): 1,625 compounds matched six of the ten different pharmacophores, while 16 optimized compounds matched two pharmacophores only (**Figure 4B**). Following D_T thresholding, 207 effective compounds were selected for molecular docking to predict their binding modes.

A similar second Phase-PBVS screen was carried out for compounds from Library 2 using Phase. First, the 1,789 FDA-approved drugs underwent ligand optimization (assignment of charges, protonation states, tautomer and chirality determination) using LigPrep[97] and Epik[98,99] modules of the Maestro software[100] (see *Methods*). This resulted in a total of 2,628 optimized drug molecules (including 839 additional confirmations), given that each of these compounds showed different protonation states, conformers, stereoisomers, and enantiomers. All 2,628 optimized drug molecules were used for PBVS to determine their PhaseScreenScore and TPS_S values. Of the 839 additional molecules, the best PhaseScreenScore value was selected reducing the library down to the 1,789 structurally optimized drug molecules (**Supp. Table 4**).

Among the 1,789 structurally optimized drugs, 906 matched to one or more pharmacophore models, 332 matched one of the ten different pharmacophores, 574 aligned with two or more pharmacophores, while 26 of those optimized drugs matched to ten pharmacophores (**Figure 4C**, and **Supp. Table 4**). Conversely, the remaining 883 drugs were excluded by the PBVS as they did not match any pharmacophores. The TPS_S values for the matching drugs ranged between 0.419 and 18.593 (**Supp. Table 4**). Subsequently, we calculated the docking threshold (D_T) values to select the compounds that will pass for the next step of molecular docking, identifying 53 effective compounds (**Figure 4D**). In this second PBVS, better PhaseScreenScore results were found for optimized molecules from Library 1 as compared to Library 2 (**Figure 4**). This is because unlike Library 1, Library 2 is smaller and it was not pre-screened with ZINCPharmer as part of the first step of PBVS. In contrast to the ZINC database, the FDA-approved dataset is much smaller and running all of the compounds for PBVS is not as computationally expensive.

A closer examination of the structural features of each pharmacophore model and the matching selected compounds from Libraries 1 and 2 suggests that the best-scored ligands adhere to 3 or 4 common point-pharmacophoric features. The APRR model was the highest-ranked pharmacophore model for the compound ZINC26876007 (PhaseScreenScore = 2.449) in Library 1 (**Supp. Table 3**). For Library 2, carvedilol was the highest-ranked, scoring best with the APR-1 model (PhaseScreenScore = 2.301) and APRR model (PhaseScreenScore = 1.736) (**Supp. Table 4**). The identification of carvedilol as a potential compound further validates our PBVS design, as carvedilol was previously reported as a MET channel blocker[36,52], despite not being included in our training set of compounds used to design the pharmacophores (**Supp. Tables 1-2**).

Predicting binding sites of known MET blockers within the pore region of TMC1

Next, we used molecular docking and molecular mechanics with generalized Born surface area (MM-GBSA) methods to predict the binding sites and affinities of 16 known MET blockers within the pore region of TMC1 (See *Methods*). These were included 13 known and chemically distinct MET blockers used as a training set to build the 3D-pharmacophore models (**Figure 1, Supp. Table 1**), supplemented with benzamil[32,37,37,101–103], tubocurarine[19,103], and DHS[17,21,104,105], which are well-known and commonly used potent MET blockers. Although commonly used in MET research, these three blockers were not included in the training set because they share some similar functional moieties with other blockers within the library of blockers, such as E6-berbamine and hexamethyleneamiloride (**Figure 1A**). Since the binding sites and modes of these 16 compounds within the pore of TMC1 remain largely unknown, we conducted a molecular docking study to predict their binding sites within the pore region.

To explore the conformational space of the TMC1 pore, docking simulations were carried out using the open-like TMC1 model we constructed, using a cube gridbox of $41_x \times 41_y \times 41_z$ Å^3 positioned to cover the transmembrane region of the pore (as identified by HOLE analysis). In these simulations, ligands were allowed to move freely without any constrain during the conformational search (**Figure 2**). The placement of the grid box is based on solid experimental evidence indicating that the pore of TMC1 is a route for both ion and small molecule uptake into hair cells. Thus, a grid box covering the chemical space of the TMC1 pore is suitable for molecular docking. Calculations were carried out with the membrane bilayer from equilibrated 25 ns MDs. Two different phospholipid molecules (referred to as POPC-A and POPC-B) neighboring the top (residues R523 and N404) and the bottom (residues T416, D419, R543, and D569) regions of the pore, were identified. These phospholipids were observed to enter the pore cavity and form a sidewall between TM4 and TM6 along the pore region (**Figure 2F, Figure 5C**, and **Figure 6G-I**), potentially modulating the accessibility and binding of small molecules with their polar and hydrophobic moieties. The use of a large 41 Å^3 gridbox allowed to explore the electronegative nature of the pore binding cavity, study its conformational space, and predict potential binding sites for the ligands (**Figure 5**).

Using the standard precision (SP) scoring function to enrich the conformational sampling of the compounds within the TMC1 pore, we predicted a total of 178 docking poses for the abovementioned list of 16 MET blockers (a docking cluster of a maximum of 10 poses per each known blocker, including the *R* and *S* stereoisomers for tubucurarine and phenoxibenzamine). These binding poses were classified according to the Emodel score[106] (see *Methods*), which reflects the quality of each cluster of docking poses obtained for each known blocker. All compounds successfully docked in three main areas of the pore, which we have named the top (**Figure 5,** *gold*), middle (**Figure 5,** *light gray*), and bottom sites (**Figure 5**, *light red*). Following the analysis of the best docking poses as ranked by the Emodel score, we identified key residues involved in binding within the pore cavity. The residues identified within the top-site of the pore include F451, E520, R523, S527, and the phospholipid POPC-B. The middle-site of the pore includes the residues M407, S408, M412, N447, D528, T531, T532 and R601. Finally, the key residues within the bottom-site of the pore include T535, D569, and the phospholipid POPC-A. A more detailed list of key binding residues is presented in **Supp. Table 5,** including key residues predicted to interact with each of 13 blockers from the training set, benzamil[32,37,101,102], tubocurarine[19,103] and DHS.

FM1-43, a positively-charged fluorescent dye commonly used to test for functional MET channels[56–58], displayed interactions across all three regions of the TMC1 cavity, particularly with residues of the TM4 and

TM5 helices (**Figure 6A**). At the top site of the pore (*gold*), FM1-43 is stacked between F451 and N404 and exhibits a 4.14 Å cation–π interaction between the positive triethylammonium group and F451 (**Figure 5D** and **6A**). The triethylammonium moiety is also surrounded by the negatively charged E458 and E520 residues, as well as by an identified zwitterionic-hydrogen bond network (referred to as ZN1 site) formed by D239, R523 and the polar head of POPC-B (along with N404) at the entrance of the pore (**Figure 6A** and **Supp. Figure 3**). The triethylammonium group also exhibits hydrophobic interactions with M403 and M407.

Within the middle site of the pore (**Figure 5,** *light gray*), the hydrophobic aromatic body of FM1-43 shows interactions with the tail of POPC-B, which stabilizes the ligand within the cavity. The benzene group of FM1-43 forms close hydrophobic contacts with residues G411 (TM4), L444 (TM5), as well as V574 and L575 (TM7). Finally, the positively charged dibutylamine group is positioned near the polar head of POPC-A, pointing to residue D569 at the bottom site of the pore (**Figure 5,** *light red*). Since both the docking and MM-GBSA methods use a dielectric field to implicitly simulate water molecules, we do not rule out the possibility that water molecules might be involved in the binding interactions of the dibutylamine group with D569 and POPC-A if simulated with explicit solvent (**Supp. Figure 3**).

The alkaloid tubocurarine exhibited interactions towards the middle and the bottom sites of the pore (**Figure 5F** and **5I**). Like FM1-43, tubocurarine displayed analogous interactions around the TM4, TM6, and TM7 domains of TMC1. The positive dimethyl-ammonium group of the tetrahydroisoquinoline moiety is proximal to the residues S408 and N447, and a hydrophobic interaction with residue F579 (TM7) within the middle site of the pore was observed (**Figure 6C**). The phenolic group linking the two tetrahydroisoquinoline scaffolds forms a hydrogen bond with residue T535 and a close contact with T531 (4.12Å) on TM6. The residue T535 is located adjacent to the second identified zwitterionic-interaction zone composed by D528, T531, T532, R601, and N580 (referred to as ZN2) (**Supp. Figure 3**). In addition, the protonatable amine of the second methyl-tetrahydroisoquinoline scaffold forms a dual salt bridge with D569 at 4.22 Å, and a hydrogen bond with the phosphate group of POPC-A at 2.82Å, a component of a third zwitterionic-interaction network at the bottom site (ZN3) (**Figure 6H**). The distances were measured between heavy atoms and the polar N^+.

For both FM1-43 and cepharanthine, docking predicted that their positively charged atoms are placed inside the pore radius measured by HOLE analysis, while some structural moieties of these molecules are docked outside the HOLE-pore contour, closer to the phospholipid wall. This suggests that ions and ligands might follow distinct permeation pathways while sharing common key amino acid residues involved in both cation and ligand binding (**Supp. Figure 4**).

Conversely, the potent benzamil blocker primarily engages in significant interactions at the bottom site (*light red*) of the pore cavity. The amine group at position 3 of the pyrazine ring forms dual hydrogen bonds with D528 and T532 (TM6). These residues, along with R601 (TM8), N598, and N580 (TM7), constitute the ZN2 site, which effectively clamps and stabilizes the pocket formed between TM6, TM7, and TM8 (**Figure 6B** and **Supp. Figure 3**). While the 6-chloropyrazine ring is located near residue N573 (TM7) and Q609 (TM8), the N-benzylcarbamimidoyl group interacts with residue M412, the location of the M412K Beethoven mutation on TM4[107], and the hydrophobic tail of POPC-A, forming van der Waals interactions.

In addition, the positively charged amidino group forms a salt bridge with D569 (2.82Å) and a hydrogen bond with the phosphate head of POPC-A at 3.1Å, which in turn establishes a hydrogen bond with T416, thereby expanding the ZN3 interactions at the bottom site (**Figure 6G** and **Supp. Figure 3**). Our results indicate that the ZN1, ZN2, and ZN3 interactions play crucial roles in ligand and TMC1 stabilization at the top (along with F451), middle, and bottom sites of the TMC1 pore, respectively.

Notably, these zwitterionic zones contain known residues implicated in ion permeation, such as D528 and D569, which are essential for ligand binding and TMC1 blockage, as well as TMC1 protein expression[84,108,109]. In addition, our results suggest that residues T532 and T535 are essential for benzamil and tubocurarine hydrogen bonding interactions, respectively.

In the absence of an experimental TMC1-blocker complex to validate our predictions, we predicted the TMC1-DHS complex interaction with high prediction accuracy using molecular docking. Our results recuperate previously reported results obtained using *in vitro* electrophysiology experiments[86,104] (**Figure 7**).

Interestingly, LigPrep and Epik predicted two main DHS charged molecules, consistent with structures reported in the literature[110,111]. One of them, with two positive charges (referred to as DHS 2^+) due to the two protonated guanidinium groups in the streptidine moiety (**Figure 7 A-C**), and the second molecule with three positive charges (referred to as DHS 3^+) includes an extra protonated *N*-methyl-*L*-glucosamine moiety (**Figure 7D-E**). DHS 2^+ displayed interactions towards the middle and bottom sites of the TMC1 pore (**Figure 7A-B**).

Like most of the middle-site interactions analyzed above, the neutral *N*-methyl-*L*-glucosamine moiety of DHS 2^+ formed double hydrogen bonds with D528 (on TM6), and the backbone carbonyl of S408 (on TM4) within the middle and bottom sites of the TMC1 pore, the hydroxyl and the guanidinium groups of the streptidine moiety show direct interactions with N573 (on TM7), D540 (on TM6), and the negatively charged head of POPC-A, respectively.

Similarly, DHS 3^+ displayed direct interactions with residues D528, S408, D540, N573, and the phospholipid of POPC-A. Additionally, the streptose moiety formed hydrogen bonds with the backbone carbonyl groups of G411 (on TM4) and G572 (on TM7), while one guanidinium group of the streptidine points towards T416 and formed direct interactions with the backbone carbonyl of M412 (on TM4). Meanwhile, the second guanidinium group interacts with the backbone carbonyl of E567.

Our results propose DHS-TMC1 interactions through residues G411, G572, S408, D540, N573, and E567. These newly predicted DHS interacting residues, along with the well-characterized M412, T416, and D528 interaction sites of DHS[86,104], further validate our docking predictions and provide high confidence to the predicted docking poses of other compounds studied in this work. Finally, our predictions also suggest that phospholipids might play a key role in DHS binding.

Effect of phospholipids on ligand binding affinities in the TMC1 pore: MM-GBSA rescoring analysis.

Next, we performed a re-scoring of the docking poses and determined the relative binding free energies (ΔG_{bind}) for the ligands using MM-GBSA in the absence of phospholipids. Additionally, since MD simulations revealed the presence of lipids, forming a lipidic sidewall between TM4 and TM6, and molecular docking indicated interactions of known blockers with both the polar heads and hydrophobic tails of theses phospholipids, we sought to investigate whether interactions with POPC-A and POPC-B modify the TMC1-ligand binding energies (**Table 2**).

As depicted in Table 2, ΔG_{bind} calculations were performed both with and without phospholipids. The results indicate that the presence of POPC-A and POPC-B generally leads to thermodynamically more favorable ΔG_{bind} energies for most of the compounds tested.

FM1-43[56–58] (**Figure 5D** and **Figure 6A**) and E6-berbamine[53], compounds with distinct structural scaffolds yet fitting similar pharmacophores (**Figure 1, Figure 3, Table 1**, and **Supp. Table 2**) exhibited the strongest binding affinities with and without phospholipids (**Table 2, Supp. Table 1**), consistent with their reported channel blocking potencies[53,56–58]. While hexamethyleneamiloride showed a slightly higher ΔG_{bind} value, UoS-7692 displayed a less negative ΔG_{bind} value, possibly due to the presence of the two fluorine substituents in acetophenone moiety at *meta* and *para* positions. Overall, our molecular docking and MM-GBSA analysis suggest that phospholipids may enhance the strength of TMC1-blocker interaction.

Binding modes and affinities of newly identified hit compounds within the TMC1 pore

We next implemented the same *in silico* strategy to the compounds obtained after PBVS from Library 1 (non-FDA-approved compounds) and the drugs from Library 2 (FDA-approved). Our initial focus was on analyzing the best 200 compounds from Library 1with the lowest MM-GBSA ΔG_{bind} values, excluding consideration of phospholipids. However, out of these compounds, only 45 were commercially available, and used for our subsequent *in silico* experiments (**Table 3, Table 4,** and **Source Data Tables 3 and 4**).

Of these 45 compounds, we selected the most structurally diverse hits using the Tanimoto-similarity coefficient[112] (See *Methods*), which revealed 15 different molecular clusters (See cluster IDs in **Table 3**). Final hit compounds from Library 1 were selected from molecular clusters that included 3 or more compounds. Specifically, three commercially available hits with the lowest ΔG_{bind} without phospholipids were selected as representatives from cluster 1.1 and 1.2, while 1 hit was selected as representative molecules from clusters 1.3 to 1.6 (**Table 3**).

Among the 53 compounds analyzed from Library 2, all commercially available, the Tanimoto-structural diversity analysis provided 10 different molecular clusters (See cluster IDs in **Table 3**). One compound was selected from each cluster with the lowest ΔG_{bind} (MM-GBSA without phospholipids).

We subsequently verified whether the selected hits identified through MM-GBSA and Tanimoto analysis without phospholipids also exhibited thermodynamically favorable MM-GBSA ΔG_{bind} energies in the presence of phospholipids. As with the known blockers (**Table 2**), MM-GBSA results in the presence of phospholipids generally showed improved ΔG_{bind} energies for hit compounds from both libraries, corroborating that the selected hits after MM-GBSA and Tanimoto analysis are listed in the top ranking in both MM-GBSA subgroups, with and without phospholipids (Table 4). Finally, 10 hits were selected from each library for experimental evaluation in cultured cochlear explants (**Table 4, Figure 8** and **Figure 10**).

Next, we analyzed the binding interactions for selected newly identified compounds within the TMC1 pore. Here, we describe interactions for some representative molecules focusing on their binding within the top, middle, and bottom sites of the pore, as guided by HOLE analysis and identified by molecular docking (**Figure 2B**). Our results are provided in the same order as presented on **Figure 6**.

Posaconazole is predicted to establish key contacts within the TMC1 pore (**Figure 6D**). We measured its molecular length using Maestro software package, which suggested an extensive molecular length of 28 Å (end-to-end distance), allowing Posaconazole to interact across the pore. At the top site, the triazole ring forms a hydrogen bond with N404 and polar interactions with the phosphate head of POPC-B at the ZN1 site. In the middle region, the dichlorophenyl-furan moiety of posaconazole stacks against M403, M407, and F451. The aromatic rings display van der Waals interactions with residues on TM5, TM6, and TM7 where the positively charged piperazine ring forms a salt bridge with D528 (3.02Å) in the ZN2 site. In the bottom site of the pore, the triazinone ring forms a hydrogen bond with N573 and the hydroxyl group interacts with D540 in the ZN3 pocket.

The non-FDA-approved compound ZINC24739924 docked at the bottom site of the pore, forming close contacts with residues of TM8 (**Figure 6E**). The ZINC24739924 benzotriazinone moiety stacks in the ZN3 pocket between the polar head of POPC-A, T535, D540, and N573. The charged triazine group makes close contacts with D540, F568, and N573. In addition, the positively charged amine forms a hydrogen bond with the phosphate group of POPC-B, while the benzyl moiety forms van der Waals contacts with M412 and the tails of both POPC-A and POPC-B, stabilizing the ligand (**Figures 6E and 6I**). Furthermore, the trifluoro-methoxy substituent exhibits polar interactions with T535 (3.16 Å) of the ZN3 site. A similar binding pattern was observed for another novel TMC1 modulator, ZINC58438263, which has a 3-methyl-anisole moiety and binds to the ZN3 site of TMC1 (**Supp. Figure 3**).

Finally, the FDA-approved drug cepharanthine shared similar interactions to those displayed by its homolog alkaloid tubocurarine within the top, middle, and bottom sites of the TMC1 pore (**Figure 6F**). At the top site, the methoxybenzene moiety displays hydrophobic interactions with N404 and polar interactions with S408 (3.98Å) on TM4. In the middle site, the aromatic rings stack towards the TM4, TM5, and TM7 domains, positioning the methylated methoxy-dihydroisoquinoline and the dioxolane moieties in between the TM5 and TM7 helices near L444 (TM5) and F579 (TM7). The second protonated dihydroisoquinoline is positioned towards the TM4 helix close to M412 (3.44Å), G411 (3.73Å), as well as the hydrophobic tail of POPC-B (3.49Å). Compared to tubocurarine, cepharanthine did not establish a direct interaction between its protonated amine and D569 or the polar head of POPC-A. However, it is possible that water molecules could facilitate these interactions at the cytoplasmic region of ZN3 (**Figure 6F**).

Identification of key residues modulating TMC1-ligand interactions

We conducted a comprehensive structural analysis of residues within a 5Å radius of each docked compound within the pore cavity to identify key TMC1-ligand interactions. This analysis included 16 known MET channel blockers, and 20 hit compounds from Libraries 1 and 2 (**Table 2, Table 4, Figure 8**), totaling 36 compounds. We analyzed all TMC1 residues lining the pore based on their contact frequency with the ligands, as determined by our docking and MM-GBSA pipeline analysis. Residues were categorized into high (>0.5) and low (<0.5) contact frequencies, indicating whether more than 50% or less than 50% of evaluated ligands interacted with each residue, respectively (**Figure 9**, with residues scoring above or below the red dashed line).

Notably, several previously characterized residues known to alter the TMC1 channel function, such as *mm*TMC1 M412, D528, T531, and D569[18,89,104,108,113–116], were among high-contact-frequency residues identified in this study. This suggests that abovementioned residues are accessible to interact with the ligands. More importantly, we also identified a set of novel residues (M407, S408, G411, P415, T416, I440, L444, N447, L524, T532, T535, G572, N573, A576, F579, M583, and R601) with contact frequencies exceeding 0.5, suggesting they are likely to be among the key residues involved in modulating the TMC1-ligand interaction.

Additionally, both POPC phospholipids showed the highest contacts frequencies, suggesting that they might play a significant role in the modulation of TMC1 function. In summary, our pipeline involving molecular docking combined with MM-GBSA has the capacity to predict high-frequency contact residues that may modulate TMC1-ligand binding across the three druggable binding sites along the TMC1 pore.

Validation of novel TMC1 modulators in cochlear hair cells using AM1-43 dye uptake assay

To validate our *in silico* findings, we conducted a fluorescent dye loading assay using FM1-43 and/or its analogue AM1-43 to assess the ability of newly identified compounds to block the MET channel in murine cochlear hair cells. Upon brief introduction into the bath solution, these large and positively-charged fluorescent dyes enter hair cells through MET channels, opened at rest. Thus, FM1-43 and AM1-43 are often used as indicators of MET channel activity, allowing us to evaluate each compound's effectiveness in interacting with the pore and modulating the dye loading through the MET channel (**Figure 10**).

For these experiments, cochlear explants from postnatal day 3 (P3) mice were cultured for two days *in vitro* at 37 °C and 8% CO_2. Then, the explants were exposed to either AM1-43 alone (positive control, supplemented with 2% DMSO) or in combination with the compound for 60 seconds, following a prior pre-incubation with the compound for another 60 seconds. After rinsing off excess dye and neutralizing any remaining background fluorescent signal with the 4-sulfonate calix[8]arene sodium salt (SCAS) quencher, live imaging of the explants was conducted using confocal microscopy.

The fluorescence intensity levels of outer hair cells were quantified individually using the Cellpose algorithm[117] and normalized to the average values measured from explants treated with AM1-43 only, separately for each experimental session. As an additional control, we incubated some cochlear explants with 100 µM tubocurarine or benzamil, two well-established potent MET channel blockers known to largely prevent FM1-43 uptake[19,101,103]. All compounds tested *in vitro* were applied at a standardized concentration of 100 µM.

Of the 20 structurally diverse hit compounds (**Table 4**), representing 10 compounds from each of the Libraries, only 15 were tested *ex vivo* due to their commercial availability. Several compounds showed a reduction of the AM1-43 dye loading through the MET channel (**Figure 10** and **Supp. Figure 5**). We used an arbitrary 60% cut-off threshold as indicative an effective blockage (**Supp. Figure 5**). From Library 1, the compounds ZINC24739924, ZINC12986242 and ZINC58438263, showed a significant reduction of AM1-43 uptake. From Library 2, posaconazole (60.02 ± 19.12%; Mean ± SD), nefazodone (68.98 ± 33.97%), pyrithioxine (also called pyritinol) (53.52 ± 30.18%), lapatinib (66.74 ± 21.65%), and cepharanthine (48.09 ± 20.72%) showed some of the best results, while ZINC06530230, suvorexant, pantoprazole, lapatinib, zeforanide, indinavir, and pantoprazole and pyritinol were less effective in reducing the AM1-43 uptake through MET channels by less than ~ 30% (**Supp. Figure 5**).

Representative compounds interacting within the top, middle, and bottom sites of the TMC1 pore chosen for illustration purposes (**Figure 6**), namely posaconazole, cepharanthine, and ZINC24739924, inhibited hair cell MET-mediated AM1-43 dye uptake by 39.98 ± 19.12 %, 54.63 ± 21.45%, and 47.07 ± 23.98%, respectively (**Figure 10**, and **Supp. Figure 5**). Overall, our results align with our *in silico* findings, indicating that compounds that were predicted to be thermodynamically favorable to interact within the TMC1 pore, showed mostly moderate, but significant reduction of AM1-43 loading when tested in cochlear hair cells. Further *in vitro* evaluation with more biological replicates followed by single-cell electrophysiology is required to carefully evaluate the potency of each hit compound. Thus, our *ex vivo* results support the efficacy of our *in silico* pipeline in identifying novel MET channel modulators within a chemical space of millions of compounds and understanding their potential binding interactions within the TMC1 pore.

Cepharanthine's dual role in TMC1 and TMEM16A modulation suggests shared pharmacophores.

Because of the structural and evolutionary relationship between the TMC and TMEM16 families of proteins[18,61,62,118], the structure and electrophysiological properties of the latter has been of great interest across multiple studies involving TMCs. Interestingly, cepharanthine, one of the most potent FDA-approved drugs in reducing the AM1-43 loading into cochlear hair cells identified in this study (**Figure 10**), has been previously reported to also inhibit TMEM16A[85,119]. Therefore, we investigated whether inhibitors of both TMC1 and TMEM16A proteins share common pharmacophoric features. To do this, we used Phase to virtually screen 10 known modulators of TMEM16A (MONNA, Ani9, TM_{inh}-23, Zafirlukast, Niclosamide, Evodiamine, Tannic acid, theaflavin, E_{act}, and F_{act})[85,119] against the 10 TMC1 pharmacophores (**Table 1**, and **Supp. Figures 2 and 4**). Our results suggest that both cepharanthine and theaflavin share the same APRR pharmacophore. Although theaflavin does not have a protonatable amine, Epik predicted a protonated carbonyl group instead (**Supp. Figure 6A-D**). In addition, the ARR-2 pharmacophore shared similar vector features between cepharanthine and the Ani9 inhibitor of TMEM16A (**Supp. Figure 6E-H**).

Our predicted docking poses for cepharanthine indicate that it binds towards the middle and bottom sites of the *mm*TMC1 pore and presents some interactions at the top site near N404 (**Figure 6F**, and **Supp. Figure E-H**). However, the binding mode of cepharanthine and theaflavin in TMEM16A was predicted and tested towards the top site of the pore[85,119].

To investigate these discrepancies, we compared the TMC1 and TMEM16A pores, carrying out a comparative structural analysis between our open-like state of the *mm*TMC1 model and the reported *mm*TMEM16 structure (PDB: 5OYB)[120] (**Supp. Figure 6I-L**). As reported in the literature, the *mm*TMEM16 structure was used to predict the binding mode of cepharanthine and theaflavin only at the top site of the pore region[85,119], equivalent to the top site within the TMC1 pore (**Supp. Figure 6I-L**). Reported docking-guided site-directed mutagenesis experiments and *in silico* MD simulations suggest that mutations at the upper binding pocket of *mm*TMEM16A attenuate the ability of cepharanthine and theaflavin to inhibit *mm*TMEM16A currents[85,121].

The predicted *mm*TMEM16A upper-binding pocket and the reported mutations can explain the decreased affinity of cepharathine and theaflavin if they only bind at the extracellular pocket of TMEM16A[121]. However, it is possible that open conformations of the *mm*TMEM16 pore might expose druggable sites at the middle and bottom areas of the pore, as we predicted for TMC1 in this study (**Figures 5 and 6, Supp. Figure 3**).

However, it is possible that the predicted docking poses for *mm*TMEM16A at its upper pocket site were biased by a closed conformation of *mm*TMEM16A and/or were restricted due to docking sampling using smaller gridboxes[85,121]. As a result, the conformational space explored in *mm*TMEM16A did not sample potential druggable sites of cepharanthine and theaflavin within the middle and bottom sites of the pore[85,121], as predicted for TMC1 in our study. This is consistent with recent reported of open-conformations of *mm*TMEM16A and newly identified druggable pocket binding sites across the pore[122,123].

Discussion

TMC1 is a nonselective cation channel which primarily passes Ca^{2+} and K^{+} into hair cells in response to mechanical stimulation. Unlike other cation channels, TMC1 lacks a conventional cylindrical pore selectivity filter[81], and instead features a long-curved pore cavity that may be partially exposed to the plasma membrane[54,88,89]. Consequently, it is significantly permeable to bulky organic molecules such as FM1-43[56,57,57], AGs[17] and others. Recent studies have even demonstrated permeation by compounds as large as 3 kDa-dextrans[124]. However, the atomic-level interactions of these compounds within the MET channel pore remains poorly understood. Furthermore, TMC1's permeability to aminoglycosides (AGs) underscores its relevance in the context of aminoglycoside-induced ototoxicity, a major concern in hearing health. Advancing our understanding of how these compounds interact within the TMC1 pore could pave the way for identifying novel otoprotective solutions to mitigate AG-induced hair cell damage in the future.

The main objective of our study was to identify the common structural features of known MET blockers and use these structural features to develop a proof-of-concept pipeline for discovering novel MET modulators, and to describe how they might interact within the TMC1 pore of the hair-cell MET channel. Our study outlines a versatile *in silico* approach to identifying novel MET channel modulators. It involves a complex multiple-selection criteria that allowed us to identify 10 novel non-FDA-approved compounds and another 10 novel FDA-approved drugs as candidates from 2 libraries that include over 230 million compounds. We performed 3D-pharmacophore modeling, AlphaFold2 modelling, molecular docking, Tanimoto similarity analysis, MM-GBSA ΔG_{bind} analysis and screened for commercial availability of hit compounds as part of our screening pipeline. Seven out of 15 hits experimentally tested compounds showed significant reduction of AM1-43 dye loading into hair cells (**Supp. Figure 5**).

Our *in silico* findings demonstrate that TMC1 possesses an expanded cavity with druggable ligand-binding sites with capacity to pass small molecules[54,125], surpassing the ion pore size reported in the literature using HOLE analysis (**Figure 2**).

The major finding of this study is that the universal 3D pharmacophore models of MET blockers we reported, are suitable to screen millions of compounds *in silico* for further testing in hair cells *in vitro*. To our knowledge, this is the first *in silico* pipeline using molecular pharmacophore modeling, docking, and MM-GBSA analysis to discover novel MET channel modulators. Furthermore, this study also identified novel atomic details of ligand interaction within the TMC1 pore, reporting a synergistic combination of amino acids forming different druggable-binding sites to accommodate for ligand interactions at the top, middle, and bottom sites of the TMC1 pore cavity.

Based on the docking poses of FM1-43 and AM1-43 (**Figure 6A**, and **Supp. Figure 3**), we infer that the tight packing of both the triethylammonium and the dibutylamine groups at the top binding site of the TMC1 pore, as well as the presence phospholipids molecules might explain why bulkier molecules like FM3-25 do not block MET currents[57], and a slow permeation property compared to fast FM1-43 uptake in hair cells[58].

The results presented in this work strongly support that the ligands bind to well-characterized residues located in the TMC1 pore, like M412, D528, T531, and D569, which have been shown to affect not only the block of DHS and FM1-43, but also the TMC1 ion permeability[18,89,104,108,113–116]. Within the new residues identified with high TMC1-ligand contact frequency interactions, some have been reported to be involved in TMC1 ion conductance path following covalent modification of cysteine side chains with the MTSET reagent[18].

Interestingly, previous studies report that mutations of the described druggable top, middle, and bottom sites involving D528, D569, and M412, cause deafness and changes in TMC1 mechanotransduction current properties *in vivo* and *in vitro*[84,107,126]. This strongly suggests that residues involved in modulation of the ion conductance might also modulate TMC1-ligand interactions. However, our docking predictions suggest a differentiation between the putative ion-conduction pathway and the ligand-permeation pathway within the TMC1 pore because chemical moieties of several docked ligands were predicted to bind in regions different than the predicted pore contour as determined by HOLE analysis (**Supp. Figure 4**).

We have identified a set of novel residues predicted to be involved in TMC1-ligand interaction. Our docking results accurately predicted several residues that interact with known MET blockers which were well

characterized experimentally in previous studies involving point mutations of TMC1 in mice[18,89,104,108,113–116]. Future studies involving site-direct mutagenesis and single-cell electrophysiology will allow to evaluate and further validate the novel contact residues identified in this study.

Our MD simulations, docking predictions, and MM-GBSA energy analyses suggest that phospholipids play a key role in small molecule binding, mediating hydrogen bonds, salt bridges, and hydrophobic interactions within the TMC1 pore (**Figure 5C,** and **5G-I, Figure 6G-I**). These findings might suggest that proper membrane function around TMC1 promotes stable ligand binding, in agreement with experimental evaluations indicating that blockage of TMC1 with high concentrations of benzamil and tubocurarine triggers membrane scrambling and phosphatidylserine externalization in hair-cell stereocilia bundles[103].

Additionally, the docking and MM-GBSA data presented here showing M412 in close contact with phospholipids, also reported as one of high-frequency ligand-binding residues, may help explain why charged mutations like M412K increase annexin V (AnV) signals, as the p.M412K mutation might attract the heads of phospholipids, promoting scrambling[103]. Our docking interactions of both benzamil and tubocurarine might also support the hypothesis of phospholipid as ligand-binding modulators (**Figure 6,** and **Supp. Fig 3**).

Since the hit compounds were evaluated in early postnatal cochlear explants (P3+2 days *in vitro*), it is conceivable that their blockage potency might be affected by the overwhelming presence of TMC2 during that developmental stage in the mouse cochlea, as TMC2 was not considered in our predictions. TMC2 is transiently expressed in mouse cochlear hair cells during early development and during onset of the hair-cell mechanotransduction, but is gradually downregulated and is replaced by TMC1 around P10[127,128]. Thus, a selective screening and design of TMC1 blockers may necessitate experimental evaluation in mature cochlear hair cells in the absence of TMC2. Since our screened compounds were based on pharmacophore models of known MET blockers, they are likely to display some blocking capability for both, TMC1 and TMC2.

This could be independently validated using TMC1-*ko* and/or TMC2-*ko* animal models. However, the structural exclusion of TMC2 from our *in silico* pipeline may promote the selection of hit candidates with possible increased selectivity for TMC1, since the putative pore of TMC2 is distinct from TMC1[129]. TMC2 pore displays a decreased hydrophobicity, smaller pore radius compared to the homologous TMC1 middle site, which might reduce the affinity of TMC2-ligand interactions[129]. It is well known that most small molecules preferentially bind to hydrophobic pockets[130]. This underscores the complexity of TMC1-blocker interactions within the druggable-pore cavity and the high variety of amino acids involved in TMC1-ligand binding. This structural complexity may suggest that the binding affinities of compounds with MET blocker properties might be TMC-isoform and -species dependent.

Thus, our study not only sheds light on the structural features required to modulate the uptake capacity of TMC1 proteins but also provides key insights on potential pharmacological relationships between TMC1 and TMEM16A proteins, since they share common 3D pharmacophores for their compound antagonists.

In summary, our combined *in silico* and *in vitro* experimental study suggest that a pharmacophore composed by two aromatic groups, one acceptor group, and at least one protonatable amine is required for blocking the TMC1 pore cavity of the hair-cell MET channel. We developed and provided a proof-of-concept validation of a pipeline for discovering novel MET channel modulators. Our pipeline successfully identified compound antagonists of the hair-cell MET function able to reduce AM1-43 loading into cochlear hair cells *in vitro*. Further evaluation of the reported compounds will shed more light on their modulatory capacities and help identify novel MET blockers, study their potential otoprotective applications, or plausible modulation of the TMEM16A function. Furthermore, future evaluation of predicted druggable high-contact sites involved in TMC1-ligand binding using site-directed mutagenesis will help to better understand their role in hair-cell mechanotransduction function, as well as their potential influence on TMC1 ion selectivity and conductance.

Materials and Methods

AlphaFold2 modeling of the MET complex structure

We generated a dimeric structural model of *Mus musculus* (*mm*) TMC1, spanning residues 81-746, adopting an open-like conformation[84] with domain swapping feature at transmembrane domain 10 (TM10). This model was constructed using AlphaFold2 through the ColabFold github repository[131]. Subsequently, the MET complex was constructed, also using AlphaFold2, by combining two TMC1 subunits, each accompanied with CIB2 (residues 1-187) and TMIE (residues 44-118) in a 1:1:1 ratio[54,132,133].

The resulting MET complex model was then compared with the structure of the expanded *C. elegans* TMC-1 complex (PDB code: 7USW)[54], showing the typical swapped conformation and location of homolog binding partners of the MET complex.

Molecular dynamics simulations

The modeled MET complex was prepared using the protein preparation wizard module of the Maestro suite[98,99,134]. Amino acid protonation states were assigned at pH 7.4 using PROPKA[135]. Subsequently, the complex was subjected to energy minimization and embedded into a pre-equilibrated POPC bilayer, followed by solvation using the SPC water model. To neutralize the system, ten K^+ ions were added, and the ion concentration was set to 0.15 M KCl. Molecular dynamics simulations were performed with Desmond[136] and the OPLS4 force field[137].

The Desmond default membrane relaxation protocol was applied before simulations. Then, 25ns-MDs in a NPγT semi-isotropic assembly were performed, applying restrictions to the protein secondary structure (spring constant 5 kcal × mol^{-1} × $Å^{-2}$) with constant surface tension of 0.0 bar × Å. Temperature and pressure were kept constant at 300 K and 1.01325 bar, respectively, by coupling to a Nose-Hoover Chain thermostat[138] and Martyna-Tobias-Klein barostat[139] with an integration time step of 2 fs.

Coulombic interactions were calculated using a cutoff of 9Å. The 25ns-MDs was analyzed with Desmond and in-house scripts. Visualization was carried out with VMD[140] and Pymol[141]. Subsequently, we analyzed the pore with the HOLE algorithm. The 25ns-MDs equilibrated structure was used for further virtual screening. In addition, we analyzed the potential location of phospholipids neighboring the TMC1 pore.

Ligand-based pharmacophore modeling of known MET blockers

Thirteen MET channel blockers with structural diversity reported in the literature such us UoS-7692[32], UoS-3607[32], UoS-3606[32], UoS-5247[32], UoS-962[32], Proto-1[91], E6-berbamine[53], hexamethyleneamiloride[36], amsacrine[36], phenoxybenzamine[36,92], carvedilol-derivate 13[52], ORC-13661[33,35], and FM1-43 (a positively charged styryl dye often used to label hair cells)[57,58], were selected to design 3D-pharmacophore models of small molecules using an energy-optimized pharmacophore method.

The pharmacophore design is a versatile approach used to extract common chemical features from a set of small molecules with biological function. First, the structures of the 13 known MET channel blockers were sketched using Maestro[100] and then prepared using LigPrep[97] (Schrödinger, 2021) with the S-OPLS force.

Salts were removed and no tautomers were generated, compound chiralities were determined from the reference 3D structure. Subsequently, both pharmacophore and ligand mapping were generated from the 13 MET blockers selected, with the Pharmacophore Alignment and Scoring Engine (Phase) module[67.] We used six pharmacophoric features: Hydrogen bond acceptor (A), hydrogen bond donor (D), hydrophobic group (H), negatively charged group (N), positively charged group (P), and aromatic ring (R).

To model the pharmacophores, a minimum of 3 and maximum of 5 pharmacophoric features were set. Also, the percentage of pharmacophore matching threshold (number of known blockers that fits to the modeled pharmacophore) of 50% was selected as a minimal criterion for a representative pharmacophore model of the 13 known MET blockers. The other settings in Phase were used by default. Finally, the best 10 pharmacophore models were ranked using the PhaseHypoScore[67]. This score measures how well the

pharmacophoric-feature vectors align with the structures of the compounds that contribute to the 3D-pharmacophore model.

Pharmacophore based virtual screening (PBVS)

In this project, we used two molecule libraries. Library 1 (non-FDA-approved compounds) from the ZINC database (ZINC20) contains over 230 million commercially available compounds in 3D formats and over 750 million purchasable analogs[93]. Library 2 (1,789 FDA-approved drugs — US Drug Collection, MicroSource Discovery Systems)[94] was in-house processed for PBVS using the LigPrep and Epik modules of Maestro[97,98,100] with the OPLS3 force field[142]. All possible ionization states were predicted for each compound at pH 7.4 ± 2.0, and their chiralities were retained.

We carried out a two-step PBVS with the non-FDA-approved Library 1. The 1st-step PBVS using the software ZINCPharmer[95], followed by a 2nd-step screening with Phase. For the ZINCPharmer screening, the 10 best pharmacophores generated after the pharmacophore mapping step were used to search the most promising compounds from ZINC20 that fits with any of the 10 pharmacophore models.

Compounds were filtered by selecting a single hit as the maximum limit per conformation for each molecule having a maximum Root Mean Square Deviation (RMSD) geometric match of 1Å against each of the 10 pharmacophore models (compounds with RMSD > 1Å were discarded). The best 50,000 hits (5,000 per each pharmacophore model) with molecular weights between 200 and 700 g/mol were selected from ZINC20. Finally, we selected the compounds that matched two or more pharmacophores using the KNIME software[143].

For the 2nd-step PBVS, the compounds from the 1st-step (Library 1) were processed with LigPrep, and ionization states were generated at pH 7.4 ± 0.5 using Epik[98,99]. In parallel, the Library 2 (FDA-approved drugs) were also processed with LigPrep and Epik. Thus, the prepared molecules from both libraries were screened against each of the 10 pharmacophores using Phase, following the methodology reported by Gallego-Yerga et al., 2021[138].

For both libraries, the PhaseScreenScore values (which evaluate how well the ligands align to the pharmacophore features of the hypothesis)[144] were obtained for each ligand per screening against each pharmacophore. In addition, we implemented a workflow with KNIME analytics platform and built a matrix to calculate the Total-PhaseScreenScore (TPS_S) for each ligand, represented by the sum of each PhaseScreenScore value. Then, we selected hits for molecular docking if the value was higher than the docking threshold (D_T) value, according to the equation 1.

$$D_T \geq \bar{X} + 2\delta \qquad \text{(Eq. 1).}$$

D_T is the docking threshold, $\bar{X}$ is the average TPS_S of the entire Library (1 or 2) solutions; and δ is the TPS_S standard deviation of the entire Library (1 or 2) solutions.

Molecular docking and free energy binding energy calculations

After PBVS, molecules from both libraries were docked with the Glide software[106] in the pore of the *mm*TMC1 model using the frame structure at 24 ns post-equilibration. The protein complex and all the phospholipids were kept for molecular docking, while waters and ions were removed. A cubic gridbox of ($41_x \times 41_y \times 41_z$) $Å^3$ was centered at methionine M412 (chain A) covering the TMC1 pore including part of the TMIE helical protein embedded in the membrane (**Figure 2**).

Molecular docking was performed for the selected hits with the best PhaseScreenScore criteria from libraries 1 and 2, overpassing the docking threshold, as well as for the 13 known MET blockers (UoS-7692, UoS-3607, UoS-3606, UoS-5247, UoS-962, Proto-1, E6-berbamine, hexamethyleneamiloride, amsacrine, phenoxybenzamine, carvedilol-derivate 13, ORC-13661 and FM1-43), benzamil, tubocurarine, and dihydrostreptomycin (DHS) (known experimental molecules used as MET channel blockers) (**Figure 1**,

Figure 5, and **Figure 7**). The Glide standard precision (SP) mode and the OPLS_2005 force field were used to explore the positional, conformational, and orientational space of the ligands in the TMC1 pore.

A maximum of 10 docking poses were requested for each ligand and the best pose was determined by selecting the conformer with the lowest Glide Emodel score followed by a low Glide Score value from superposed-like poses[106]. The Glide Emodel was prioritized, since Glide uses Emodel to pick the best pose of a ligand (conformer selection) and subsequently rank them against one another using GlideScore[106]. A manual check of each representative pose was carried out to identify common binding sites for each selected pose from each molecular docking cluster.

Molecular docking solutions from both libraries 1 and 2 were rescored by calculating their binding free energies (ΔG_{Bind}). Two docking postprocessing strategies were implemented. Strategy A: excluding phospholipids neighboring the pore, and strategy B: including key phospholipids neighboring the pore that could influence small molecule binding. ΔG_{Bind} calculations were carried out using the molecular mechanics−generalized Born surface area (MM-GBSA) method[145] with Prime[146], combining molecular mechanics energies and implicit solvation models[147]. The MM-GBSA ΔG_{Bind} between ligands and the TMC1 channel was calculated with the following equations:

$$\Delta G_{bind} = \Delta H - T\Delta S \approx \Delta E_{MM} + \Delta G_{sol} - T\Delta S, \quad \text{(Eq. 2)}$$

$$\Delta E_{MM} = \Delta E_{internal} + \Delta E_{electrostatic} + \Delta E_{vdw};\ \Delta G_{sol} = \Delta G_{PB/GB} + \Delta G_{SA}, \quad \text{(Eq. 3)}$$

where ΔE_{MM}, ΔG_{sol}, and $-T\Delta S$ are the changes in the molecular mechanics energy, solvation-free energy, and conformational entropy upon binding, respectively. ΔE_{MM} includes $\Delta E_{internal}$ (bond, angle, and dihedral energies), electrostatic, and van der Waals energies. ΔG_{sol} is the sum of the electrostatic solvation energy, $\Delta G_{PB/GB}$ (polar contribution), and non-electrostatic solvation, ΔG_{SA} (non-polar contribution). The polar contribution was calculated by using the generalized born model, while the non-polar energy was calculated by the solvent accessible surface area (SASA). The VSGB 2.0[148] solvation model and OPLS force field were used for these calculations. Residues located within 5Å from the ligands were included in the flexible region, and the rest of the protein atoms were kept frozen.

Morgan fingerprint and Tanimoto-similarity coefficient

After virtual screening through both libraries, Morgan fingerprint similarity factors[149] were determined for all molecules with the RDKit module of the KNIME analytics platform. This extended-connectivity fingerprint based on Morgan algorithm represent molecules as mathematical objects, which allow us to analyze the structural environment of each atom up to a radius of 2Å[149]. Using the Morgan fingerprint, we calculated the distance matrix with the Tanimoto-similarity coefficient[112], which allowed us to determine the structural similarity of the compounds on a scale from 0 (non-identical) to 1 (identical).

Then hierarchical clustering was performed with the average linkage method. Clusters were selected using the normalized distance threshold of 0.75 for the non-FDA-approved dataset (Library 1) and 0.85 for the FDA-approved dataset (Library 2) to enhance structural diversity. Representative compounds for populated clusters were selected for further evaluation.

Mouse cochlear explant cultures

All animal procedures were approved by Mass Eye and Ear Institutional Animal Care and Use Committee. Postnatal day (P) 3 CD-1 mice of either sex were cryo-anesthetized and euthanized by decapitation. Inner ears were harvested and organ of Corti epithelia were acutely dissected in Leibovitz's L-15 (Invitrogen) cell culture medium. Following dissection, explants were affixed to glass-bottom cell culture dishes coated with Geltrex basement membrane matrix (#A1569601, 100 μL/dish) and cultured in DMEM (#12430054) supplemented with 3% FBS and 10 mg/L ampicillin for 48 hours at 37 °C, 8% CO_2.

Dye loading and fluorescence imaging

Following gentle aspiration of the culture medium at room temperature, the explants were rinsed with L15 and were pre-treated for 60 s with the compound at a final concentration of 100 μM (dissolved in L15 at 2% DMSO). Following another 60 s of incubation with the hit compound, the solution was aspirated and replaced with a solution consisting of the loading dye AM1-43 (4 μM) and the hit compound (100 μM) of in L15 with 2% DMSO). AM1-43 was used instead of FM1-43 to allow imaging of fixed tissue should such a need arise, but all samples included in this study were imaged live.

Following another 60 s of incubation, the solution was aspirated, and the excess AM1-43 dye was neutralized using a quenching solution composed of 0.2 mM SCAS (Biotium) in L-15. The dye-only control solution was composed of 4 μM AM1-43 in L15 at 2% DMSO. Imaging of the samples was performed using a Leica SP5 confocal microscope equipped with a 40×, 0.8 NA water-dipping objective lens with a zoom was set to 2×, resulting in an effective pixel size 189*189 nm. The laser power and smart gain settings were kept constant across all experimental conditions. During each experimental session, at least one compound and one control sample were imaged.

Image analysis

Following image acquisition, maximum intensity Z-projections were generated using ImageJ. Subsequently, Cellpose[117] was used to segment individual outer hair cells (OHC) into regions of interest (ROIs). The mean fluorescence intensity of each OHC was then quantified and normalized to the average fluorescence intensity level of the corresponding control OHCs treated with AM1-43 (4 μM) in L15 and 2% DMSO.

Acknowledgments

We want to tank Dr. Angela Ballesteros (NIDCD) for her valuable scientific feedback and critical reading of the manuscript draft, and Carlos Peña-Varas (Universidad de Concepción – Chile) for advice on figure visualization.

Funding

This work was supported by NIH R01DC020190 (NIDCD) and R01DC017166 (NIDCD) to A.A.I, and the Speech and Hearing Bioscience and Technology Program Training grant T32 DC000038 (NIDCD), as well as Chilean National Research and Development Agency (ANID), Fondecyt 1220656, 1230446, and FOVI210027. The funders had no role in study design, data collection and analysis, decision to publish, or preparation of the manuscript.

References

1. Angeli, S., Lin, X. & Liu, X. Z. Genetics of Hearing and Deafness. *Anat. Rec. Hoboken NJ 2007* **295**, 1812–1829 (2012).
2. Bitner-Glindzicz, M. Hereditary deafness and phenotyping in humans. *Br. Med. Bull.* **63**, 73–94 (2002).
3. Cornejo-Sanchez, D. M. *et al.* Rare-variant association analysis reveals known and new age-related hearing loss genes. *Eur. J. Hum. Genet.* **31**, 638–647 (2023).
4. Noise and Hearing Loss: A Review - Daniel - 2007 - Journal of School Health - Wiley Online Library. https://onlinelibrary.wiley.com/doi/abs/10.1111/j.1746-1561.2007.00197.x.
5. Kros, C. J. & Steyger, P. S. Aminoglycoside- and Cisplatin-Induced Ototoxicity: Mechanisms and Otoprotective Strategies. *Cold Spring Harb. Perspect. Med.* **9**, a033548 (2019).
6. Wang, X. *et al.* Cisplatin-induced ototoxicity: From signaling network to therapeutic targets. *Biomed. Pharmacother.* **157**, 114045 (2023).
7. Le, T. A. *et al.* Aminoglycoside-Related Nephrotoxicity and Ototoxicity in Clinical Practice: A Review of Pathophysiological Mechanism and Treatment Options. *Adv. Ther.* **40**, 1357–1365 (2023).
8. Rybak, L. P., Ramkumar, V. & Mukherjea, D. Ototoxicity of Non-aminoglycoside Antibiotics. *Front. Neurol.* **12**, 652674 (2021).
9. O'Sullivan, M. E. *et al.* Dissociating antibacterial from ototoxic effects of gentamicin C-subtypes. *Proc. Natl. Acad. Sci. U. S. A.* **117**, 32423–32432 (2020).
10. Huth, M. E., Ricci, A. J. & Cheng, A. G. Mechanisms of Aminoglycoside Ototoxicity and Targets of Hair Cell Protection. *Int. J. Otolaryngol.* **2011**, 937861 (2011).
11. Bitner-Glindzicz, M. & Rahman, S. Ototoxicity caused by aminoglycosides. *BMJ* **335**, 784–785 (2007).
12. Fischel-Ghodsian, N. Genetic factors in aminoglycoside toxicity. *Pharmacogenomics* **6**, 27–36 (2005).
13. Zhao, H. *et al.* Maternally inherited aminoglycoside-induced and nonsyndromic deafness is associated with the novel C1494T mutation in the mitochondrial 12S rRNA gene in a large Chinese family. *Am. J. Hum. Genet.* **74**, 139–152 (2004).
14. Rybak, L. P. & Ramkumar, V. Ototoxicity. *Kidney Int.* **72**, 931–935 (2007).
15. Steyger, P. S. Mechanisms of Ototoxicity and Otoprotection. *Otolaryngol. Clin. North Am.* **54**, 1101–1115 (2021).
16. Vu, A. A. *et al.* Integrity and Regeneration of Mechanotransduction Machinery Regulate Aminoglycoside Entry and Sensory Cell Death. *PLoS ONE* **8**, e54794 (2013).
17. Marcotti, W., Van Netten, S. M. & Kros, C. J. The aminoglycoside antibiotic dihydrostreptomycin rapidly enters mouse outer hair cells through the mechano -electrical transducer channels. *J. Physiol.* **567**, 505–521 (2005).
18. Pan, B. *et al.* TMC1 Forms the Pore of Mechanosensory Transduction Channels in Vertebrate Inner Ear Hair Cells. *Neuron* **99**, 736-753.e6 (2018).
19. Kirkwood, N. K. *et al.* d-Tubocurarine and Berbamine: Alkaloids That Are Permeant Blockers of the Hair Cell's Mechano-Electrical Transducer Channel and Protect from Aminoglycoside Toxicity. *Front. Cell. Neurosci.* **11**, (2017).
20. Alharazneh, A. *et al.* Functional Hair Cell Mechanotransducer Channels Are Required for Aminoglycoside Ototoxicity. *PLOS ONE* **6**, e22347 (2011).
21. Ohmori, H. Mechano-electrical transduction currents in isolated vestibular hair cells of the chick. *J. Physiol.* **359**, 189–217 (1985).
22. Kazmierczak, P. *et al.* Cadherin 23 and protocadherin 15 interact to form tip-link filaments in sensory hair cells. *Nature* **449**, 87–91 (2007).
23. Kachar, B., Parakkal, M., Kurc, M., Zhao, Y. & Gillespie, P. G. High-resolution structure of hair-cell tip links. *Proc. Natl. Acad. Sci. U. S. A.* **97**, 13336–13341 (2000).
24. Jaiganesh, A. *et al.* Zooming in on Cadherin-23: Structural Diversity and Potential Mechanisms of Inherited Deafness. *Structure* **0**, (2018).
25. Siemens, J. *et al.* Cadherin 23 is a component of the tip link in hair-cell stereocilia. *Nature* **428**, 950–955 (2004).
26. Dionne, G. *et al.* Mechanotransduction by PCDH15 Relies on a Novel cis-Dimeric Architecture. *Neuron* **99**, 480-492.e5 (2018).
27. Choudhary, D. *et al.* Structural determinants of protocadherin-15 mechanics and function in hearing and balance perception. *Proc. Natl. Acad. Sci.* (2020) doi:10.1073/pnas.1920444117.
28. Ahmed, Z. M. *et al.* The tip-link antigen, a protein associated with the transduction complex of sensory hair cells, is protocadherin-15. *J. Neurosci. Off. J. Soc. Neurosci.* **26**, 7022–7034 (2006).
29. Maeda, R. *et al.* Tip-link protein protocadherin 15 interacts with transmembrane channel-like proteins TMC1 and TMC2. *Proc. Natl. Acad. Sci. U. S. A.* **111**, 12907–12912 (2014).
30. Mulhall, E. M. *et al.* Single-molecule force spectroscopy reveals the dynamic strength of the hair-cell tip-link connection. *Nat. Commun.* **12**, 849 (2021).
31. Arora, N. *et al.* Emergence of slip-ideal-slip behavior in tip-links serve as force filters of sound in hearing. *Nat. Commun.* **15**, 1595 (2024).
32. Kenyon, E. J. *et al.* Identification of a series of hair-cell MET channel blockers that protect against aminoglycoside-induced ototoxicity. *JCI Insight* **6**, e145704 (2021).
33. Kitcher, S. R. *et al.* ORC-13661 protects sensory hair cells from aminoglycoside and cisplatin ototoxicity. *JCI Insight* **4**, (2019).
34. Nekrassov, V. & Sitges, M. Vinpocetine protects from aminoglycoside antibiotic-induced hearing loss in guinea pig in vivo. *Brain Res.* **868**, 222–229 (2000).

35. Chowdhury, S. *et al.* Phenotypic Optimization of Urea–Thiophene Carboxamides To Yield Potent, Well Tolerated, and Orally Active Protective Agents against Aminoglycoside-Induced Hearing Loss. *J. Med. Chem.* **61**, 84–97 (2018).
36. Ou, H. C. *et al.* Identification of FDA-Approved Drugs and Bioactives that Protect Hair Cells in the Zebrafish (Danio rerio) Lateral Line and Mouse (Mus musculus) Utricle. *J. Assoc. Res. Otolaryngol.* **10**, 191–203 (2009).
37. Vlasits, A. L., Simon, J. A., Raible, D. W., Rubel, E. W. & Owens, K. N. Screen of FDA-approved drug library reveals compounds that protect hair cells from aminoglycosides and cisplatin. *Hear. Res.* **294**, 153–165 (2012).
38. Breglio, A. M. *et al.* Cisplatin is retained in the cochlea indefinitely following chemotherapy. *Nat. Commun.* **8**, 1654 (2017).
39. Guo, J., Chai, R., Li, H. & Sun, S. Protection of Hair Cells from Ototoxic Drug-Induced Hearing Loss. in *Hearing Loss: Mechanisms, Prevention and Cure* (eds. Li, H. & Chai, R.) 17–36 (Springer, Singapore, 2019). doi:10.1007/978-981-13-6123-4_2.
40. Hsieh, C.-Y. *et al.* Otoprotection against aminoglycoside- and cisplatin-induced ototoxicity focusing on the upstream drug uptake pathway. *J. Chin. Med. Assoc.* 10.1097/JCMA.0000000000001023 (2024) doi:10.1097/JCMA.0000000000001023.
41. O'Sullivan, M. E. & Cheng, A. G. Mind Your Ears: A New Antidote to Aminoglycoside Toxicity? *J. Med. Chem.* **61**, 81–83 (2018).
42. Lee, J., Fernandez, K. & Cunningham, L. L. Hear and Now: Ongoing Clinical Trials to Prevent Drug-Induced Hearing Loss. *Annu. Rev. Pharmacol. Toxicol.* **64**, 211–230 (2024).
43. FDA, D. A. and D. FDA approves sodium thiosulfate to reduce the risk of ototoxicity associated with cisplatin in pediatric patients with localized, non-metastatic solid tumors. *FDA* (2022).
44. Brock, P. R. *et al.* Sodium Thiosulfate for Protection from Cisplatin-Induced Hearing Loss. *N. Engl. J. Med.* **378**, 2376–2385 (2018).
45. Safety - There's only one PEDMARK. *PEDMARK® (sodium thiosulfate injection)* https://www.pedmark.com/safety/.
46. Deng, G. Reducing Aminoglycoside Ototoxicity. (2012).
47. Wang, J. *et al.* Local application of sodium thiosulfate prevents cisplatin-induced hearing loss in the guinea pig. *Neuropharmacology* **45**, 380–393 (2003).
48. Schroeder, R. J., Audlin, J., Luo, J. & Nicholas, B. D. Pharmacokinetics of sodium thiosulfate in Guinea pig perilymph following middle ear application. *J. Otol.* **13**, 54–58 (2018).
49. Saito, T., Zhang, Z. J., Manabe, Y., Ohtsubo, T. & Saito, H. The effect of sodium thiosulfate on ototoxicity and pharmacokinetics after cisplatin treatment in guinea pigs. *Eur. Arch. Otorhinolaryngol.* **254**, 281–286 (1997).
50. Berglin, C. E. *et al.* Prevention of cisplatin-induced hearing loss by administration of a thiosulfate-containing gel to the middle ear in a guinea pig model. *Cancer Chemother. Pharmacol.* **68**, 1547–1556 (2011).
51. Dhillon, S. Sodium Thiosulfate: Pediatric First Approval. *Pediatr. Drugs* **25**, 239–244 (2023).
52. O'Reilly, M. *et al.* Design, Synthesis, and Biological Evaluation of a New Series of Carvedilol Derivatives That Protect Sensory Hair Cells from Aminoglycoside-Induced Damage by Blocking the Mechanoelectrical Transducer Channel. *J. Med. Chem.* **62**, 5312–5329 (2019).
53. Kruger, M. *et al.* Natural Bizbenzoquinoline Derivatives Protect Zebrafish Lateral Line Sensory Hair Cells from Aminoglycoside Toxicity. *Front. Cell. Neurosci.* **10**, 83 (2016).
54. Jeong, H. *et al.* Structures of the TMC-1 complex illuminate mechanosensory transduction. *Nature* **610**, 796–803 (2022).
55. Pan, B., Waguespack, J., Schnee, M. E., LeBlanc, C. & Ricci, A. J. Permeation properties of the hair cell mechanotransducer channel provide insight into its molecular structure. *J. Neurophysiol.* **107**, 2408–2420 (2012).
56. Derudas, M. *et al.* Charge and lipophilicity are required for effective block of the hair-cell mechano-electrical transducer channel by FM1-43 and its derivatives. *Front. Cell Dev. Biol.* **11**, 1247324 (2023).
57. Gale, J. E., Marcotti, W., Kennedy, H. J., Kros, C. J. & Richardson, G. P. FM1-43 Dye Behaves as a Permeant Blocker of the Hair-Cell Mechanotransducer Channel. *J. Neurosci.* **21**, 7013–7025 (2001).
58. Meyers, J. R. *et al.* Lighting up the senses: FM1-43 loading of sensory cells through nonselective ion channels. *J. Neurosci. Off. J. Soc. Neurosci.* **23**, 4054–4065 (2003).
59. Gund, P. Three-Dimensional Pharmacophoric Pattern Searching. in *Progress in Molecular and Subcellular Biology* (eds. Hahn, F. E., Kersten, H., Kersten, W. & Szybalski, W.) 117–143 (Springer, Berlin, Heidelberg, 1977). doi:10.1007/978-3-642-66626-1_4.
60. Seidel, T., Schuetz, D. A., Garon, A. & Langer, T. The Pharmacophore Concept and Its Applications in Computer-Aided Drug Design. *Prog. Chem. Org. Nat. Prod.* **110**, 99–141 (2019).
61. Medrano-Soto, A. *et al.* Bioinformatic characterization of the Anoctamin Superfamily of Ca2+-activated ion channels and lipid scramblases. *PLoS ONE* **13**, e0192851 (2018).
62. Hahn, Y., Kim, D. S., Pastan, I. H. & Lee, B. Anoctamin and transmembrane channel-like proteins are evolutionarily related. *Int. J. Mol. Med.* **24**, 51–55 (2009).
63. Structural relationship between the putative hair cell mechanotransduction channel TMC1 and TMEM16 proteins | eLife. https://elifesciences.org/articles/38433.
64. Zhang, M. *et al.* Structure of the mechanosensitive OSCA channels. *Nat. Struct. Mol. Biol.* **25**, 850 (2018).
65. Schaller, D. *et al.* Next generation 3D pharmacophore modeling. *WIREs Comput. Mol. Sci.* **10**, e1468 (2020).
66. Ambure, P., Kar, S. & Roy, K. Pharmacophore mapping-based virtual screening followed by molecular docking studies in search of potential acetylcholinesterase inhibitors as anti-Alzheimer's agents. *Biosystems* **116**, 10–20 (2014).

67. Dixon, S. L., Smondyrev, A. M. & Rao, S. N. PHASE: a novel approach to pharmacophore modeling and 3D database searching. *Chem. Biol. Drug Des.* **67**, 370–372 (2006).
68. Yang, S.-Y. Pharmacophore modeling and applications in drug discovery: challenges and recent advances. *Drug Discov. Today* **15**, 444–450 (2010).
69. Ferreira, L. G., Dos Santos, R. N., Oliva, G. & Andricopulo, A. D. Molecular Docking and Structure-Based Drug Design Strategies. *Molecules* **20**, 13384–13421 (2015).
70. Nada, H. *et al.* Perspective for Discovery of Small Molecule IL-6 Inhibitors through Study of Structure–Activity Relationships and Molecular Docking. *J. Med. Chem.* **66**, 4417–4433 (2023).
71. Ren, F. *et al.* AlphaFold accelerates artificial intelligence powered drug discovery: efficient discovery of a novel CDK20 small molecule inhibitor. *Chem. Sci.* **14**, 1443–1452 (2023).
72. Dutt, M. *et al.* Drug repurposing for Mpox: Discovery of small molecules as potential inhibitors against DNA-dependent RNA polymerase using molecular modeling approach. *J. Cell. Biochem.* **124**, 701–715 (2023).
73. Peitzika, S.-C. & Pontiki, E. A Review on Recent Approaches on Molecular Docking Studies of Novel Compounds Targeting Acetylcholinesterase in Alzheimer Disease. *Molecules* **28**, 1084 (2023).
74. Asiamah, I., Obiri, S. A., Tamekloe, W., Armah, F. A. & Borquaye, L. S. Applications of molecular docking in natural products-based drug discovery. *Sci. Afr.* **20**, e01593 (2023).
75. Agu, P. C. *et al.* Molecular docking as a tool for the discovery of molecular targets of nutraceuticals in diseases management. *Sci. Rep.* **13**, 13398 (2023).
76. Kitchen, D. B., Decornez, H., Furr, J. R. & Bajorath, J. Docking and scoring in virtual screening for drug discovery: methods and applications. *Nat. Rev. Drug Discov.* **3**, 935–949 (2004).
77. Malkaje, S., Srinivasa, M. G., Deshpande N, S., Navada, S., & Revanasiddappa BC. An In-silico Approach: Design, Homology Modeling, Molecular Docking, MM/GBSA Simulations, and ADMET Screening of Novel 1,3,4-oxadiazoles as PLK1inhibitors. *Curr. Drug Res. Rev. Former. Curr. Drug Abuse Rev.* **15**, 88–100 (2023).
78. Basnet, S., Ghimire, M. P., Lamichhane, T. R., Adhikari, R. & Adhikari, A. Identification of potential human pancreatic α-amylase inhibitors from natural products by molecular docking, MM/GBSA calculations, MD simulations, and ADMET analysis. *PLOS ONE* **18**, e0275765 (2023).
79. Singh, A. P., Ahmad, S., Raza, K. & Gautam, H. K. Computational screening and MM/GBSA-based MD simulation studies reveal the high binding potential of FDA-approved drugs against Cutibacterium acnes sialidase. *J. Biomol. Struct. Dyn.* **0**, 1–11 (2023).
80. Ramírez, D. *et al.* Discovery of Novel TASK-3 Channel Blockers Using a Pharmacophore-Based Virtual Screening. *Int. J. Mol. Sci.* **20**, 4014 (2019).
81. Ramírez, D. *et al.* 5-(Indol-2-yl)pyrazolo[3,4-b]pyridines as a New Family of TASK-3 Channel Blockers: A Pharmacophore-Based Regioselective Synthesis. *Molecules* **26**, 3897 (2021).
82. Gálvez, J. *et al.* Design, facile synthesis, and evaluation of novel spiro- and pyrazolo[1,5-c]quinazolines as cholinesterase inhibitors: Molecular docking and MM/GBSA studies. *Comput. Biol. Chem.* **74**, 218–229 (2018).
83. De-la-Torre, P. *et al.* A Novel Class of Selective Acetylcholinesterase Inhibitors: Synthesis and Evaluation of (E)-2-(Benzo[d]thiazol-2-yl)-3-heteroarylacrylonitriles. *Molecules* **17**, 12072–12085 (2012).
84. Akyuz, N. *et al.* Mechanical gating of the auditory transduction channel TMC1 involves the fourth and sixth transmembrane helices. *Sci. Adv.* **8**, eabo1126.
85. Zhang, X. *et al.* Cepharanthine, a novel selective ANO1 inhibitor with potential for lung adenocarcinoma therapy. *Biochim. Biophys. Acta BBA - Mol. Cell Res.* **1868**, 119132 (2021).
86. Beurg, M. *et al.* New Tmc1 Deafness Mutations Impact Mechanotransduction in Auditory Hair Cells. *J. Neurosci.* **41**, 4378–4391 (2021).
87. Murthy, S. E. *et al.* OSCA/TMEM63 are an evolutionarily conserved family of mechanically activated ion channels. *eLife* **7**, e41844 (2018).
88. Giese, A. P. J. *et al.* Complexes of vertebrate TMC1/2 and CIB2/3 proteins form hair-cell mechanotransduction cation channels. *eLife* **12**, (2023).
89. Walujkar, S. *et al.* In Silico Electrophysiology of Inner-Ear Mechanotransduction Channel TMC1 Models. 2021.09.17.460860 Preprint at https://doi.org/10.1101/2021.09.17.460860 (2021).
90. Smart, O. S., Neduvelil, J. G., Wang, X., Wallace, B. A. & Sansom, M. S. HOLE: a program for the analysis of the pore dimensions of ion channel structural models. *J. Mol. Graph.* **14**, 354–60, 376 (1996).
91. Owens, K. N. *et al.* Identification of Genetic and Chemical Modulators of Zebrafish Mechanosensory Hair Cell Death. *PLOS Genet.* **4**, e1000020 (2008).
92. Majumder, P., Moore, P. A., Richardson, G. P. & Gale, J. E. Protecting Mammalian Hair Cells from Aminoglycoside-Toxicity: Assessing Phenoxybenzamine's Potential. *Front. Cell. Neurosci.* **11**, (2017).
93. Irwin, J. J. & Shoichet, B. K. ZINC – A Free Database of Commercially Available Compounds for Virtual Screening. *J. Chem. Inf. Model.* **45**, 177–182 (2005).
94. MicroSource Discovery Systems, Inc. - The US Drug Collection. http://www.msdiscovery.com/usdrug.html.
95. Koes, D. R. & Camacho, C. J. ZINCPharmer: pharmacophore search of the ZINC database. *Nucleic Acids Res.* **40**, W409-414 (2012).
96. Zhang, M. *et al.* Pharmacophore Modeling, Synthesis, and Antibacterial Evaluation of Chalcones and Derivatives. *ACS Omega* **3**, 18343–18360 (2018).
97. Life Science: LigPrep. *Schrödinger* https://newsite.schrodinger.com/platform/products/ligprep/.
98. Shelley, J. C. *et al.* Epik: a software program for pKaprediction and protonation state generation for drug-like molecules. *J. Comput. Aided Mol. Des.* **21**, 681–691 (2007).
99. Epik, S. Protein Preparation Wizard. Epik: Schrödinger, LLC, New York, NY. Schrödinger, LLC. (2019).

100. Maestro, Schrödinger. Schrödinger (2021).
101. Vélez-Ortega, A. C., Freeman, M. J., Indzhykulian, A. A., Grossheim, J. M. & Frolenkov, G. I. Mechanotransduction current is essential for stability of the transducing stereocilia in mammalian auditory hair cells. *eLife* **6**, e24661.
102. Rüsch, A., Kros, C. J. & Richardson, G. P. Block by amiloride and its derivatives of mechano-electrical transduction in outer hair cells of mouse cochlear cultures. *J. Physiol.* **474**, 75–86 (1994).
103. Ballesteros, A. & Swartz, K. J. Regulation of membrane homeostasis by TMC1 mechanoelectrical transduction channels is essential for hearing. *Sci. Adv.* **8**, eabm5550 (2022).
104. Corns, L. F., Johnson, S. L., Kros, C. J. & Marcotti, W. Tmc1 Point Mutation Affects Ca2+ Sensitivity and Block by Dihydrostreptomycin of the Mechanoelectrical Transducer Current of Mouse Outer Hair Cells. *J. Neurosci.* **36**, 336–349 (2016).
105. Kroese, A. B. A., Das, A. & Hudspeth, A. J. Blockage of the transduction channels of hair cells in the bullfrog's sacculus by aminoglycoside antibiotics. *Hear. Res.* **37**, 203–217 (1989).
106. Friesner, R. A. *et al.* Glide: a new approach for rapid, accurate docking and scoring. 1. Method and assessment of docking accuracy. *J. Med. Chem.* **47**, 1739–1749 (2004).
107. Vreugde, S. *et al.* Beethoven, a mouse model for dominant, progressive hearing loss DFNA36. *Nat. Genet.* **30**, 257–258 (2002).
108. Fettiplace, R., Furness, D. N. & Beurg, M. The conductance and organization of the TMC1-containing mechanotransducer channel complex in auditory hair cells. *Proc. Natl. Acad. Sci.* **119**, e2210849119 (2022).
109. Corey, D. P., Akyuz, N. & Holt, J. R. Function and Dysfunction of TMC Channels in Inner Ear Hair Cells. *Cold Spring Harb. Perspect. Med.* **9**, a033506 (2019).
110. Hansen, F. A. & Pedersen-Bjergaard, S. Electromembrane extraction of streptomycin from biological fluids. *J. Chromatogr. A* **1639**, 461915 (2021).
111. Blundell, C. D., Packer, M. J. & Almond, A. Quantification of free ligand conformational preferences by NMR and their relationship to the bioactive conformation. *Bioorg. Med. Chem.* **21**, 4976–4987 (2013).
112. Rácz, A., Bajusz, D. & Héberger, K. Life beyond the Tanimoto coefficient: similarity measures for interaction fingerprints. *J. Cheminformatics* **10**, 48 (2018).
113. Beurg, M., Goldring, A. C. & Fettiplace, R. The effects of Tmc1 Beethoven mutation on mechanotransducer channel function in cochlear hair cells. *J. Gen. Physiol.* **146**, 233–243 (2015).
114. Beurg, M., Barlow, A., Furness, D. N. & Fettiplace, R. A Tmc1 mutation reduces calcium permeability and expression of mechanoelectrical transduction channels in cochlear hair cells. *Proc. Natl. Acad. Sci.* **116**, 20743–20749 (2019).
115. Holt, J. R. *et al.* Putting the Pieces Together: the Hair Cell Transduction Complex. *JARO J. Assoc. Res. Otolaryngol.* **22**, 601–608 (2021).
116. Goldring, A. C., Beurg, M. & Fettiplace, R. The contribution of TMC1 to adaptation of mechanoelectrical transduction channels in cochlear outer hair cells. *J. Physiol.* **597**, 5949–5961 (2019).
117. Stringer, C., Wang, T., Michaelos, M. & Pachitariu, M. Cellpose: a generalist algorithm for cellular segmentation. *Nat. Methods* **18**, 100–106 (2021).
118. Ballesteros, A., Fenollar-Ferrer, C. & Swartz, K. J. Structural relationship between the putative hair cell mechanotransduction channel TMC1 and TMEM16 proteins. *eLife* **7**, e38433 (2018).
119. Al-Hosni, R., Ilkan, Z., Agostinelli, E. & Tammaro, P. The pharmacology of the TMEM16A channel: therapeutic opportunities. *Trends Pharmacol. Sci.* **43**, 712–725 (2022).
120. Paulino, C., Kalienkova, V., Lam, A. K. M., Neldner, Y. & Dutzler, R. Activation mechanism of the calcium-activated chloride channel TMEM16A revealed by cryo-EM. *Nature* **552**, 421–425 (2017).
121. Shi, S., Ma, B., Sun, F., Qu, C. & An, H. Theaflavin binds to a druggable pocket of TMEM16A channel and inhibits lung adenocarcinoma cell viability. *J. Biol. Chem.* **297**, (2021).
122. Shi, S. *et al.* Identification of a druggable pocket of the calcium-activated chloride channel TMEM16A in its open state. *J. Biol. Chem.* **299**, 104780 (2023).
123. Jia, Z. & Chen, J. Specific PIP2 binding promotes calcium activation of TMEM16A chloride channels. *Commun. Biol.* **4**, 1–10 (2021).
124. Ballesteros, A. & Swartz, K. J. Dextran Labeling and Uptake in Live and Functional Murine Cochlear Hair Cells. *J. Vis. Exp. JoVE* (2020) doi:10.3791/60769.
125. Farris, H. E., LeBlanc, C. L., Goswami, J. & Ricci, A. J. Probing the pore of the auditory hair cell mechanotransducer channel in turtle. *J. Physiol.* **558**, 769–792 (2004).
126. Zhao, Y. *et al.* A novel DFNA36 mutation in TMC1 orthologous to the Beethoven (Bth) mouse associated with autosomal dominant hearing loss in a Chinese family. *PloS One* **9**, e97064 (2014).
127. Kurima, K. *et al.* TMC1 and TMC2 Localize at the Site of Mechanotransduction in Mammalian Inner Ear Hair Cell Stereocilia. *Cell Rep.* **12**, 1606–1617 (2015).
128. Ratzan, E. M. *et al.* TMC function, dysfunction, and restoration in mouse vestibular organs. *Front. Neurol.* **15**, (2024).
129. Clark, S., Jeong, H., Posert, R., Goehring, A. & Gouaux, E. Structure of C. elegans TMC-2 complex suggests roles of lipid-mediated subunit contacts in mechanosensory transduction. *BioRxiv Prepr. Serv. Biol.* 2023.08.16.553618 (2023) doi:10.1101/2023.08.16.553618.
130. Guo, Z. *et al.* Identification of Protein–Ligand Binding Sites by the Level-Set Variational Implicit-Solvent Approach. *J. Chem. Theory Comput.* **11**, 753–765 (2015).

131. Mirdita, M., Ovchinnikov, S. & Steinegger, M. ColabFold - Making protein folding accessible to all. 2021.08.15.456425 Preprint at https://doi.org/10.1101/2021.08.15.456425 (2021).
132. Giese, A. P. J. *et al.* CIB2 interacts with TMC1 and TMC2 and is essential for mechanotransduction in auditory hair cells. *Nat. Commun.* **8**, 43 (2017).
133. Liang, X. *et al.* CIB2 and CIB3 are auxiliary subunits of the mechanotransduction channel of hair cells. *Neuron* **109**, 2131-2149.e15 (2021).
134. Jacobson, M. P., Friesner, R. A., Xiang, Z. & Honig, B. On the Role of the Crystal Environment in Determining Protein Side-chain Conformations. *J. Mol. Biol.* **320**, 597–608 (2002).
135. Olsson, M. H. M., Søndergaard, C. R., Rostkowski, M. & Jensen, J. H. PROPKA3: Consistent Treatment of Internal and Surface Residues in Empirical pKa Predictions. *J. Chem. Theory Comput.* **7**, 525–537 (2011).
136. Bowers, K. J. *et al.* Scalable Algorithms for Molecular Dynamics Simulations on Commodity Clusters. in *SC '06: Proceedings of the 2006 ACM/IEEE Conference on Supercomputing* 43–43 (2006). doi:10.1109/SC.2006.54.
137. Lu, C. *et al.* OPLS4: Improving Force Field Accuracy on Challenging Regimes of Chemical Space. *J. Chem. Theory Comput.* **17**, 4291–4300 (2021).
138. Gallego-Yerga, L. *et al.* Application of ensemble pharmacophore-based virtual screening to the discovery of novel antimitotic tubulin inhibitors. *Comput. Struct. Biotechnol. J.* **19**, 4360–4372 (2021).
139. Martyna, G. J., Tobias, D. J. & Klein, M. L. Constant pressure molecular dynamics algorithms. *J. Chem. Phys.* **101**, 4177–4189 (1994).
140. Humphrey, W., Dalke, A. & Schulten, K. VMD: Visual molecular dynamics. *J. Mol. Graph.* **14**, 33–38 (1996).
141. DeLano, W. L. Pymol. (2002).
142. Harder, E. *et al.* OPLS3: A Force Field Providing Broad Coverage of Drug-like Small Molecules and Proteins. *J. Chem. Theory Comput.* **12**, 281–296 (2016).
143. Berthold, M. R. *et al.* KNIME - the Konstanz information miner: version 2.0 and beyond. *ACM SIGKDD Explor. Newsl.* **11**, 26–31 (2009).
144. Structure-Based Virtual Screening Using Phase Workshop Tutorial | Schrödinger. https://www.schrodinger.com/training/structure-based-virtual-screening-using-phase-workshop-tutorial221.
145. Hou, T., Wang, J., Li, Y. & Wang, W. Assessing the Performance of the MM/PBSA and MM/GBSA Methods. 1. The Accuracy of Binding Free Energy Calculations Based on Molecular Dynamics Simulations. *J. Chem. Inf. Model.* **51**, 69–82 (2011).
146. Prime, Schrödinger, LLC, New York, NY, USA. (2017).
147. Kaminski, G. A., Friesner, R. A., Tirado-Rives, J. & Jorgensen, W. L. Evaluation and Reparametrization of the OPLS-AA Force Field for Proteins via Comparison with Accurate Quantum Chemical Calculations on Peptides. *J. Phys. Chem. B* **105**, 6474–6487 (2001).
148. Li, J. *et al.* The VSGB 2.0 model: a next generation energy model for high resolution protein structure modeling. *Proteins* **79**, 2794–2812 (2011).
149. Rogers, D. & Hahn, M. Extended-Connectivity Fingerprints. *J. Chem. Inf. Model.* **50**, 742–754 (2010).

FIGURES, FIGURE LEGENDS, AND TABLES

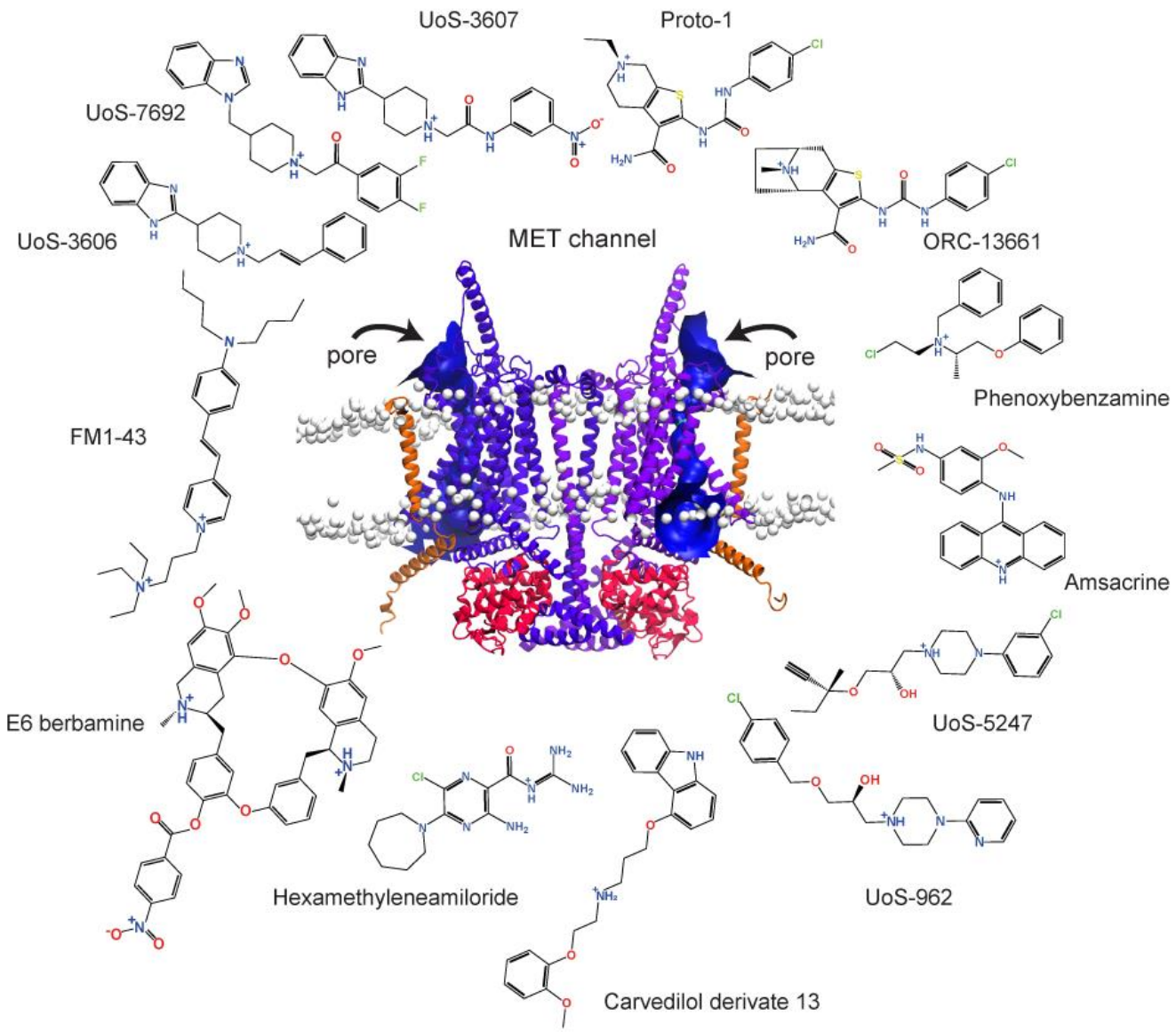

Figure 1. Structural diversity of known MET blockers. Compounds reported to display varied MET channel blocker potencies and AG protection (Supp Table 1). These compounds share a protonatable nitrogen atom and at least one aromatic ring in their structures. Potential protonatable nitrogen atoms are marked with a blue sphere with a plus sign. Front view a of our dimeric TMC1 model (purple) in complex with two protomers of TMIE (orange) and two protomers of CIB2 (red) proteins. Heads of phospholipids are showed as white beads. Arrows represent the entry site of small molecules via the pores in both TMC1 protomers calculated by HOLE[90] (blue). More details about this model are presented in Figure 2 and in the Methods section.

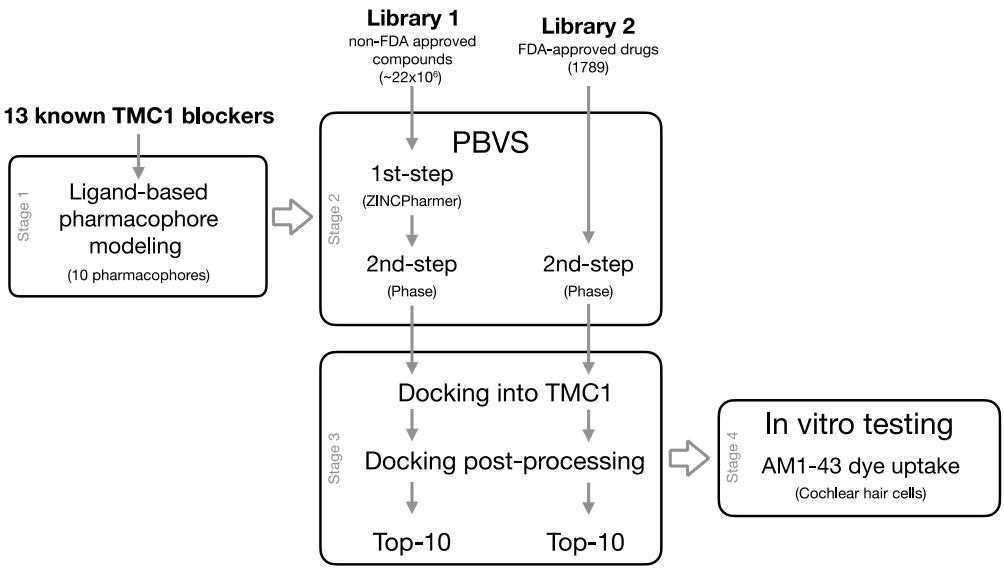

Scheme 1. Systematic workflow employed to identify TMC1 modulators. Initially, 10 commercially available top hit compounds were selected from each of two libraries: Library 1 (ZINC Database)[93] and Library 2 (MicroSource Discovery Systems)[94] resulting in a total of 20 hit compounds (see *Methods* for details).

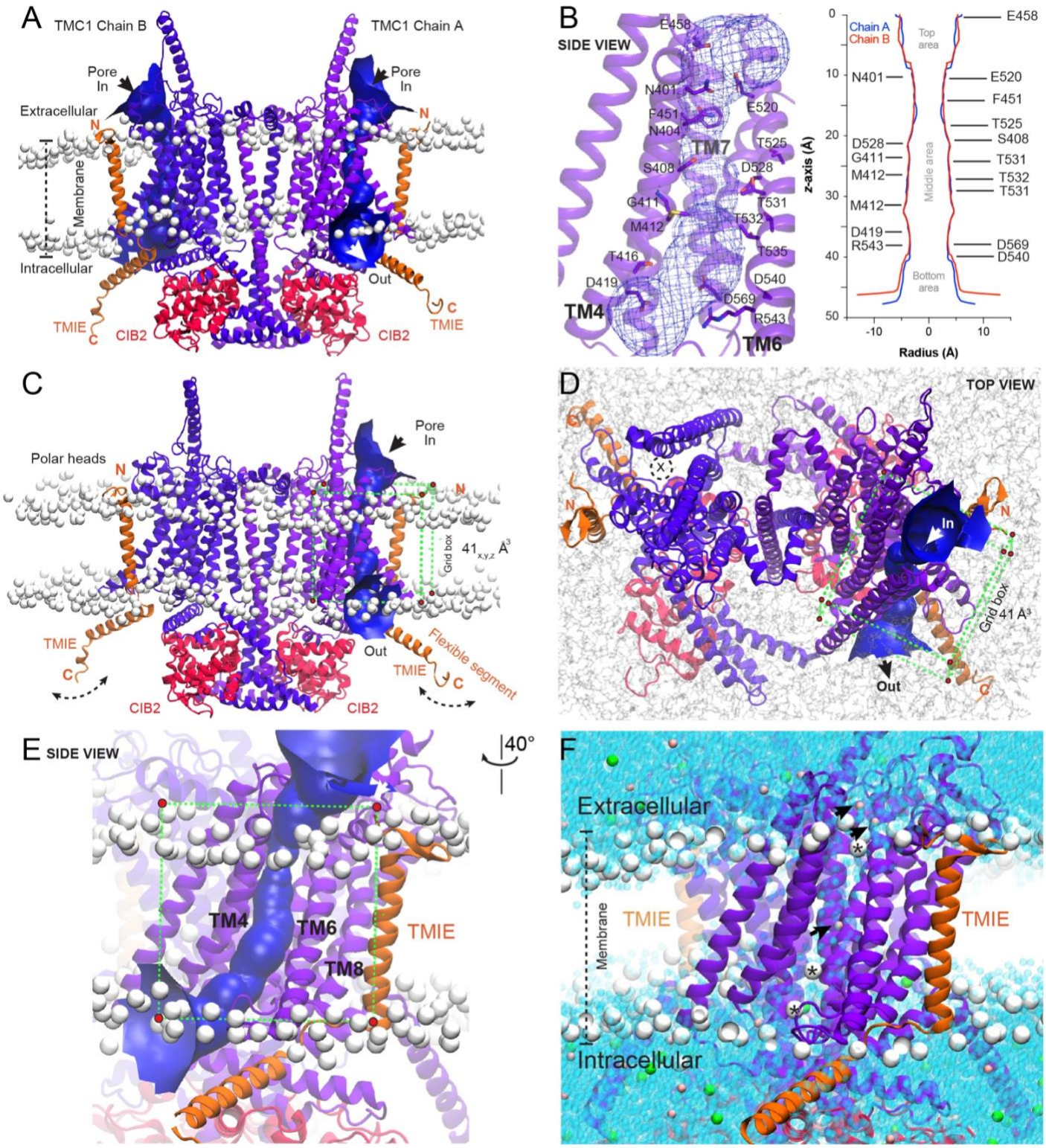

Figure 2. TMC1 modeling and molecular dynamics simulations. We built a dimeric open-like conformation of the TMC1 structure using AlphaFold2. **(A)** Front view of a 25 ns frame of the dimeric, equilibrated TMC1 protein in complex with two protomers of TMIE (orange) and two protomers of CIB2 (red) proteins. The system is embedded in a POPC membrane, with the phospholipid heads illustrated as white beads. The TMC1 pores of chain A and B are represented by a blue funnel obtained by HOLE[90] analysis. **(B)** Detailed view of the TMC1 pore of chain A, depicting the pore in a mesh representation, and amino acids as purple sticks. The inset depicts the van der Waals radius (Å) of the pore plotted against the distance (Å) along the pore of both TMC1 chains (*z*-axis), obtained by HOLE[90] analysis. Top, middle, and bottom areas of the pore are labeled according to the most expanded regions of the pore. **(C)** Front view of the complex as in panel *a*. The flexible TMIE C-terminal segment is labeled (see *Supp. Figure 1*). A 41 Å^3 docking gridbox is represented by green dashed lines with vertices in red circles. **(D)** Top view of the simulated system showing the swapped TMC1 conformation with two pores represented by a blue surface (chain A) and a dashed circle with an X (chain B), respectively. Same gridbox as in panel *c*. **(E)** Zoomed-in side view of chain A from panel C showing the gridbox and TM domains forming the pore. **(F)** Zoomed-in side view of the MET complex showing water molecules filling the pore (blue beads). K^+ ions are illustrated as pink beads, while Cl^- ions as green beads. K^+ ions visiting the pore are pointed with black arrows. Phospholipids that moved into the pore are indicated by asterisks (see *Supp. Figure 3*).

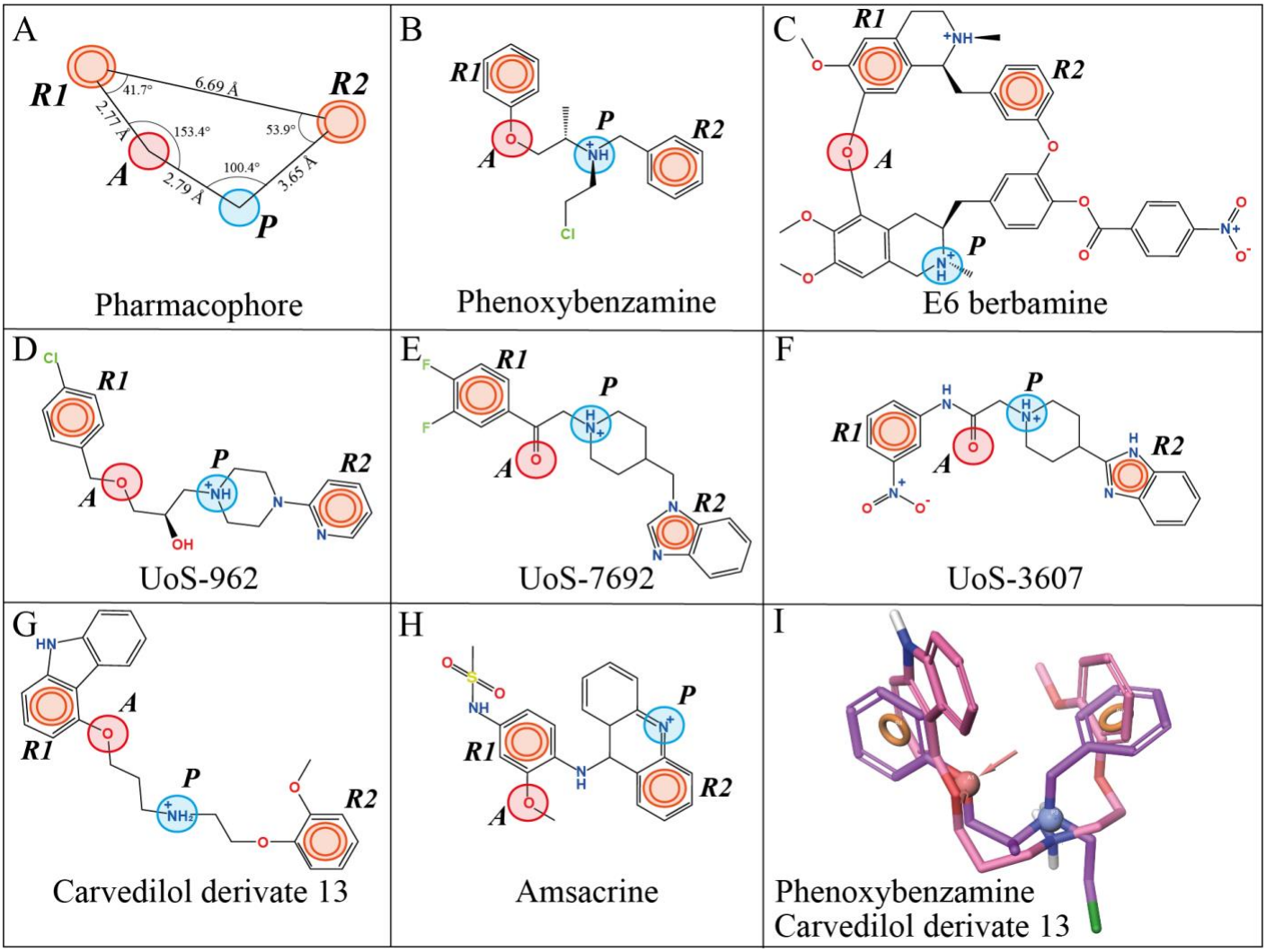

Figure 3. Pharmacophore modeling of 13 known MET channel blockers. **(A)** The APRR four-point pharmacophore model of MET channel modulators show a hydrogen-bond acceptor feature (*A*) in red, two aromatic rings (*R1* and *R2*) in orange, and a positively charged group (*P*) in blue. Distances and angles between the pharmacophoric features are labeled. This model showed the highest PhaseHypoScore (APRR = 0.780) matching 7 out of 13 matching blockers. **(B–H)** A 2D-representation of the APRR pharmacophore model with matching compounds. **(I)** Superposed 3D-structures of the MET blockers phenoxybenzamine (purple) and carvedilol derivative 13 (pink) onto the APRR pharmacophore. These two compounds fit all 10 pharmacophores reported in Table 1 (see also Supp. Table 2).

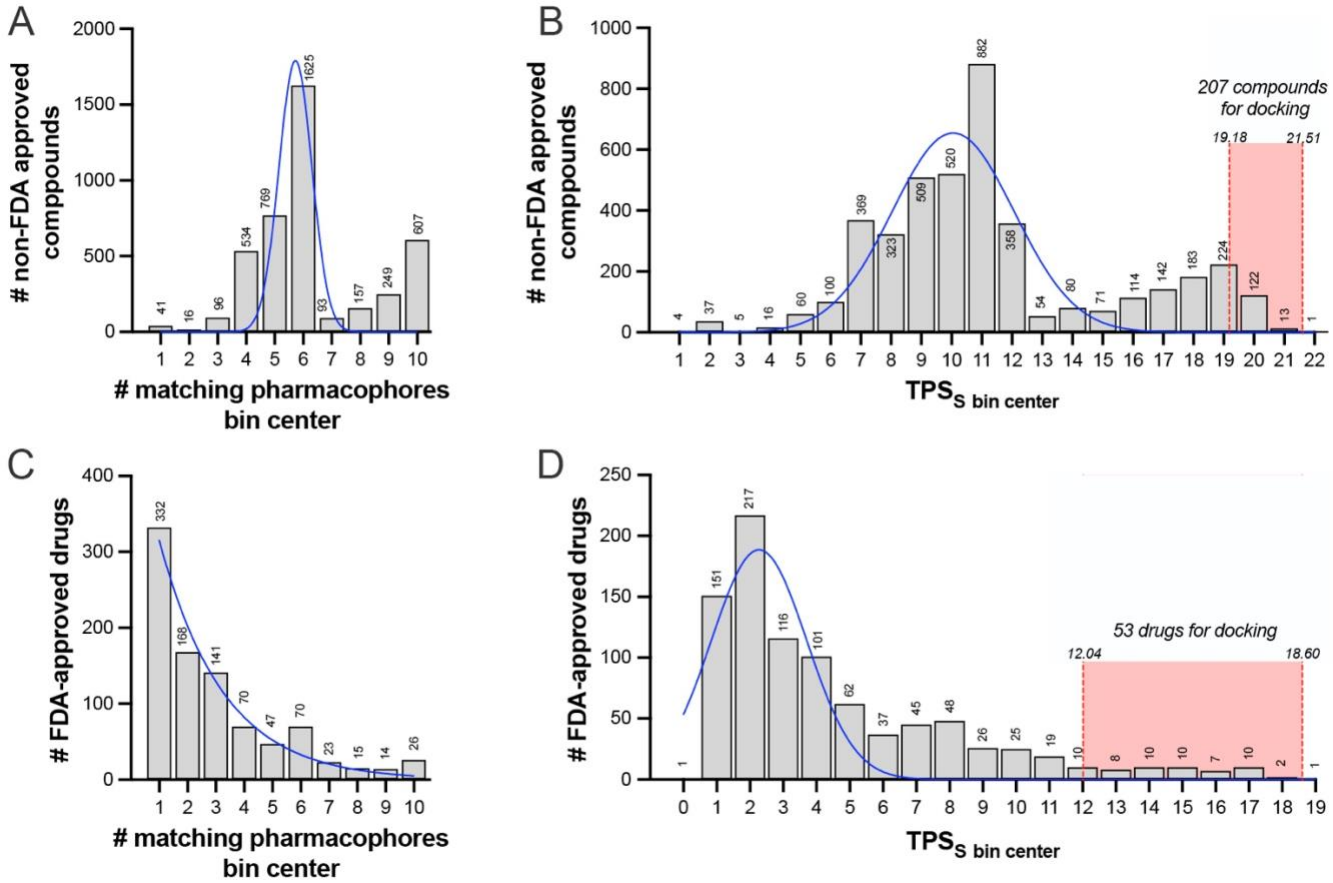

Figure 4. Second step PBVS analysis results for Libraries 1 and 2. (A) Histogram reporting the number of compounds presented as a function of the number of pharmacophores they matched following the second step PBVS in Phase. **(B)** Frequency distribution of non-FDA-approved compounds from Library 1 as a function of their Total-PhaseScreenScore (*TPSs*). Red shaded area represents the compounds with *TPSs* score values above the cut-off docking threshold (Mean + 2 SD) as a selection criterion. **(C)** Histogram reporting the number of FDA-approved compounds presented as a function of the number of pharmacophores they matched following PVBS in Phase. **(D)** Frequency distribution of FDA-approved drugs from Library 2 as a function of their *TPSs*. Red shaded area represents the compounds with *TPSs* score values above the cut-off docking threshold (Mean + 2 SD) as a selection criterion. Values above the bars report the number of compounds per bin. Blue lines represent the data fit for normal (Gaussian) distribution.

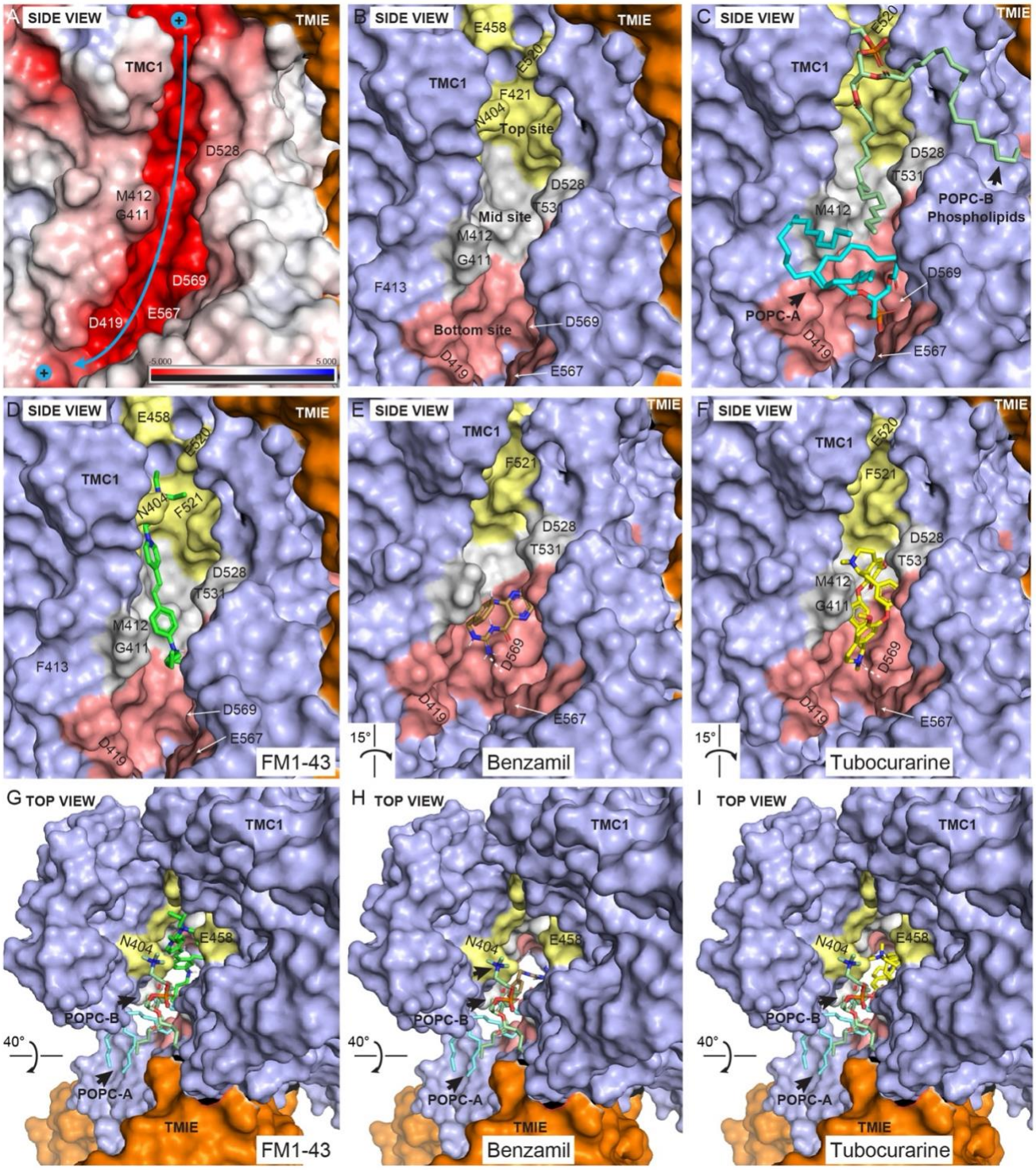

Figure 5. Molecular docking of known blockers within the TMC1 pore cavity. Side view surface representation of TMC1 chain A pore (*light purple*). TMIE is shown as an orange surface, while CIB2 is not displayed for clarity. **(A)** Surface electrostatic potential (calculated by PyMOL) of TMC1 cavity. Electronegative area is highlighted in red, electropositive in blue, and hydrophobic in white. The cavity of TMC1 is highly electronegative with a cation pathway indicated by the *blue arrow*. **(B)** TMC1 pore cavity highlighting 3 ligand-binding sites: top (*gold*), middle (*light gray*), and bottom (*light red*) sites of the pore, color-coded for illustration purposes. Binding at these sites is governed by interactions between the positively charged amine group of the ligands with residues E458 and F451 (*top site*), D528 (*middle site*), and D569 (*bottom site*), as well as hydrophobic and hydrogen bond interactions with other residues within the TMC1 pore cavity. **(C)** Side view, similar to panel B, showing the location of two key phospholipids (POPC-A and POPC-B) identified during MD simulations. The polar head of POPC-A points towards the bottom site forming a zwitterionic-like interaction network near D569, key for ligand binding. Additionally, the polar head of POPC-B forms a similar zwitterionic-like network with R523 at the top site (see also *Figure 6* and *Supp. Figure 3*). **(D)** Binding interaction of FM1-43 (*green*) across the top, middle, and near the bottom sites of the pore. **I** Binding interaction of benzamil (*brown*) at the bottom site of the pore. Dashed white line represents a hydrogen bond interaction with D569. **(F)** Binding interaction of tubocurarine (*yellow*) at the middle and the bottom sites of the pore. Dashed white line as in panel E. (**G-I)** Top views of FM1-43, benzamil, and tubocurarine showing the location of the ligands and the phospholipid sidewall formed by POPC-A and POPC-B surrounding the ligands. Additional illustrations on interactions are presented in *Figure 6* and *Supp. Figure 4*.

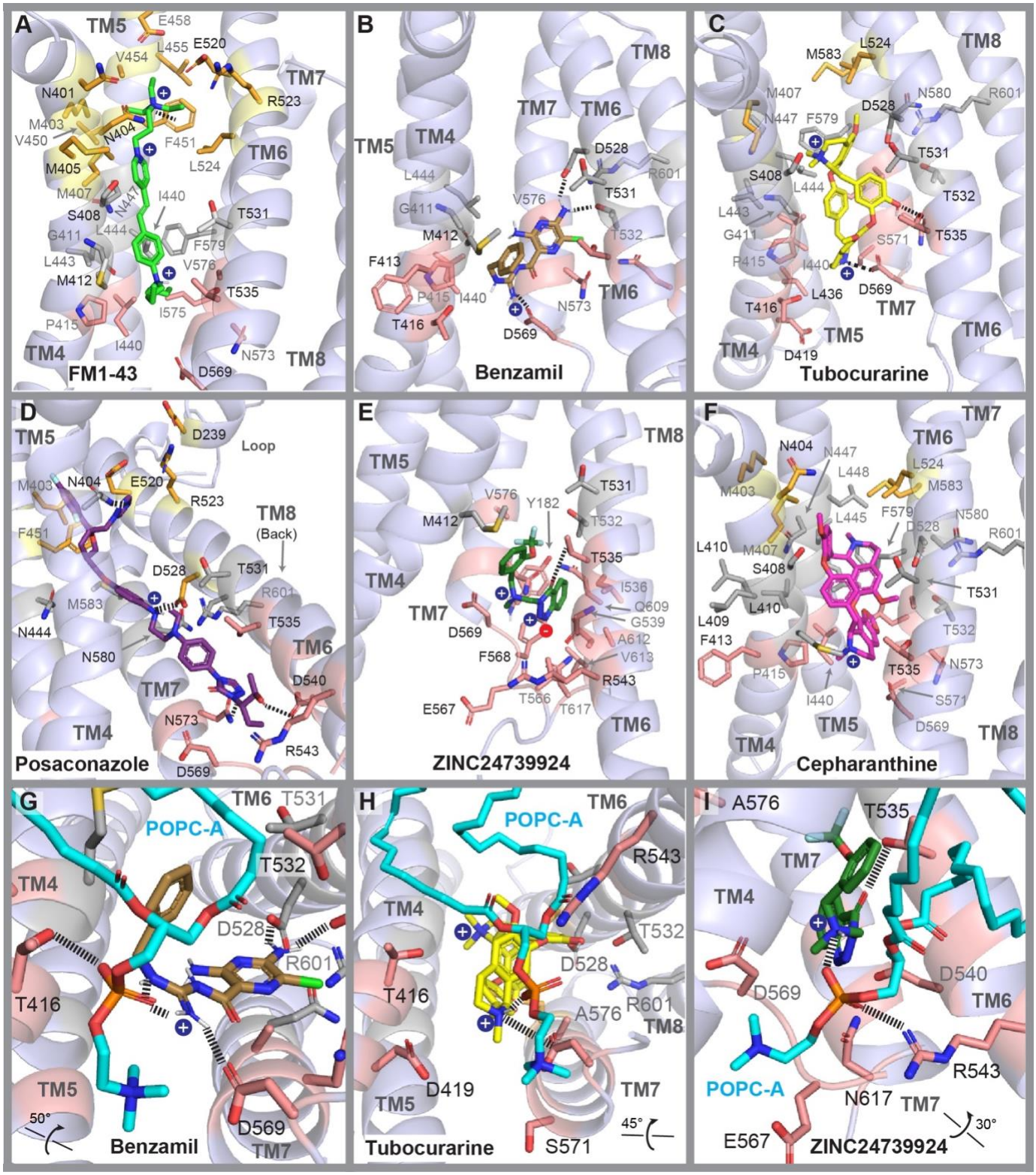

Figure 6. Molecular docking simulations of known and novel TMC1 blockers. Cartoon representation and binding modes of blockers. **(A)** FM1-43 (*green*) within the cavity of TMC1 (*light purple*). **(B)** Benzamil (*brown*). **(C)** Tubocurarine (*yellow*). **(D)** Posaconazole (*dark purple*). **(E)** Compound ZINC24739924 (*green*). **(F)** Cepharanthine (*magenta*). **(G-I)** Bottom view of the ZN3 bottom site with benzamil, tubocurarine, and compound ZINC24739924, respectively. Residues are labeled in *black* and *gray* for their position at the front or at the back of each helix, respectively. The side chains and the backbone residues are colored as in *Figure 5*, according to their location within the top (*gold*), middle (*light gray*), and bottom (*light red*) sites of the TMC1 pore. Residues within 5Å distance from each blocker are displayed, and key interactions highlighted with black dashed lines. Additional illustrations on interactions are presented in *Supp. Figure 4*.

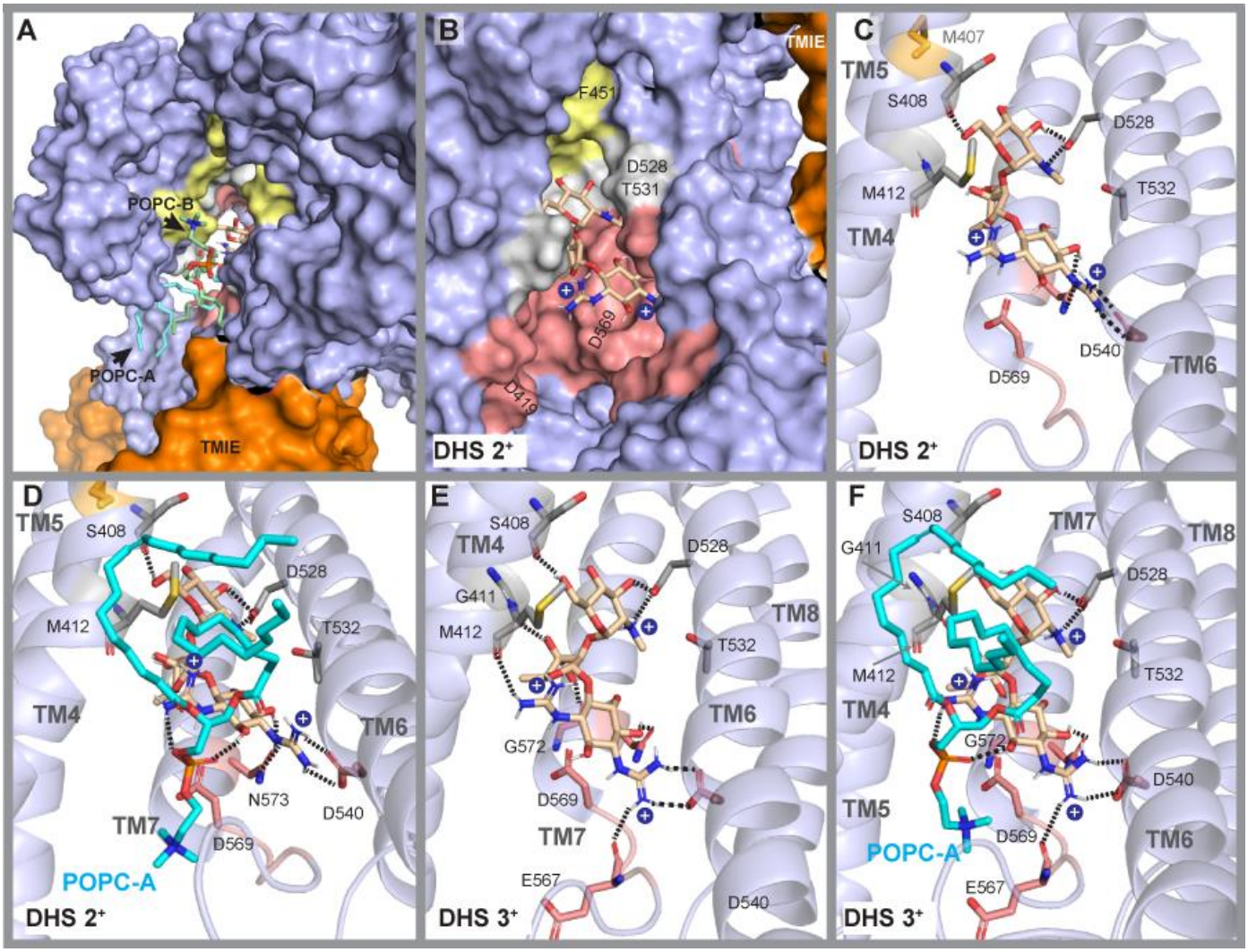

Figure 7. Molecular docking of dihydrostreptomycin (DHS) within the TMC1 pore. Binding interactions following molecular docking and MM-GBSA. Phospholipids are not displayed in some panels to visualize DHS and TMC1 only. Each positively charged nitrogen is shown as a blue bead. Dashed lines represent direct hydrogen bonds or salt-bridge interactions. **(A)** Top view of DHS (2^+) showing the location of the ligand and the phospholipid sidewall formed by POPC-A and POPC-B, surrounding the ligands. **(B)** Side view of DHS (2^+) within the TMC1 pore. Top site (*gold*), middle site (*light gray*), and bottom site (*light red*) are shown. Phospholipids are not displayed for clarity. Binding at these sites is governed by interactions between the positively charged amine and guanidinium groups, as well as the hydroxyl groups of DHS (2^+) with amino acids of the middle and bottom sites. **(C)** Docking pose of DHA (2^+) showing hydrogen bonds between the *N*-methyl-*L*-glucosamine head with the amino acids S408 and D528. The streptose moiety pointed towards TM7, while the guanidinium groups of the streptidine moiety displayed hydrogen bond interactions with N573 and salt bridges with D540. One of the guanidinium groups points to D569 in a region exposed to solvent (*more details in panel D*). **(D)** Bottom view from panel C. Interactions between DHS (2^+), TMC1, and POPC-A within the bottom site of the pore cavity. One guanidinium group displayed interactions with N573 and D540 (*as in panel C*), while the second guanidinium group showed interactions with the polar head of POPC-A. **(E)** Side view of DHS (3^+) within the pore showing interactions similar to DHS (2^+). Additionally, the hydroxyl group of the streptose moiety formed hydrogen bonds with the carbonyl backbone groups of G411 and G572, while the guanidinium groups formed hydrogen bonds with the carbonyl backbone groups of M412 and E567. **(F)** Interactions of DHS (3^+) within the pore and with POPC-A.

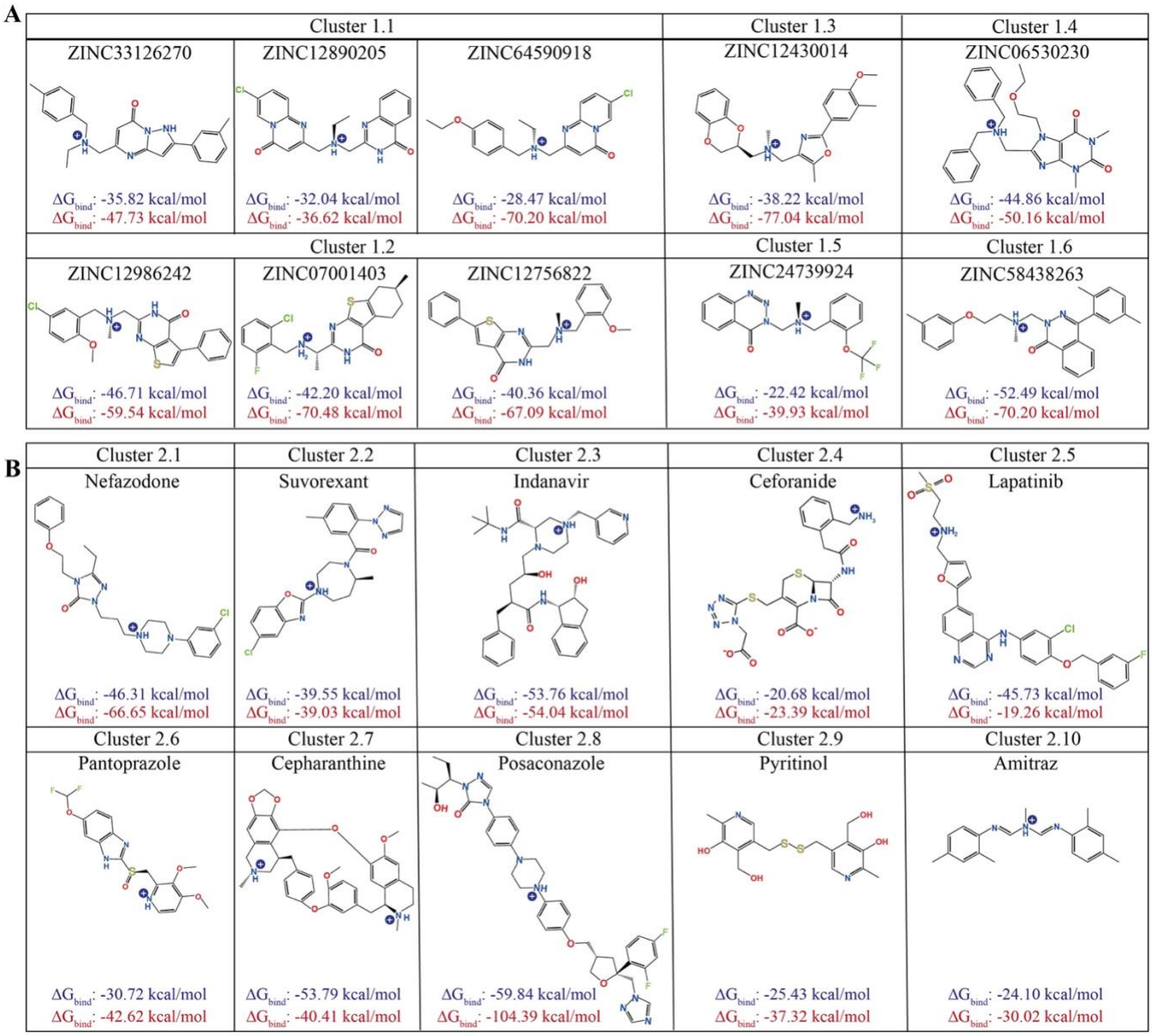

Figure 8. **List of final hits selected for experimental evaluation.** (A) Chemical structures of the 10 selected hits from Library 1 (non-FDA-approved). (B) Chemical structures of the 10 selected hits from Library 2 (FDA-approved drugs). The calculated MM-GBSA ΔG_{bind} energies are shown for all selected hit compounds in blue (without POPCs) and in red (with POPCs), respectively. Compounds were sketched using ChemDraw.

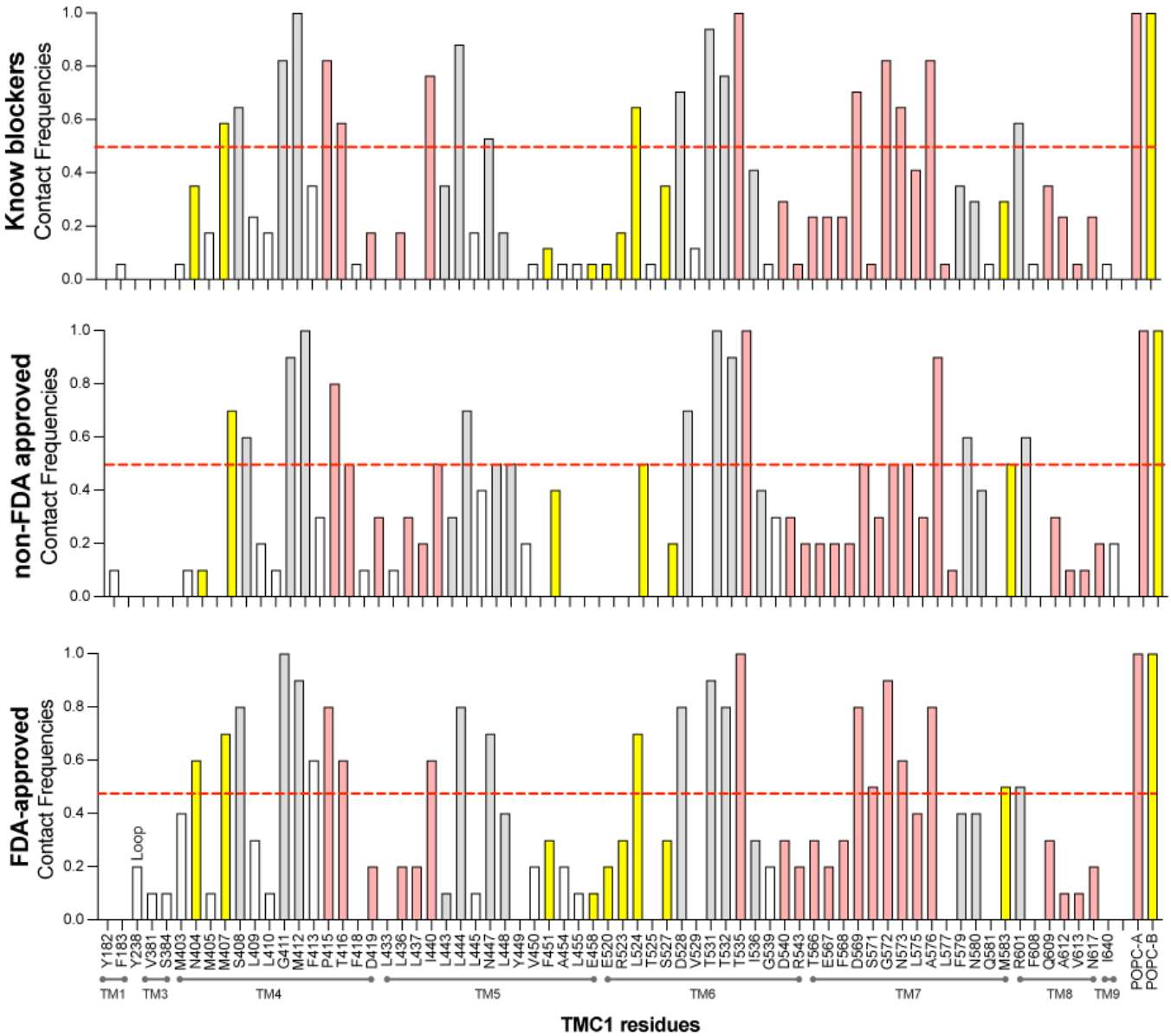

Figure 9. Contact frequencies of residues involved in TMC1-ligand binding across 36 analyzed compounds. Contact frequencies, representing the portion of ligands interacting with the respective residue. Frequency columns are colored according to the location of the residue within the top (*gold*), middle (*light gray*), and bottom (*light red*) sites of the TMC1 pore. White columns indicate residues not identified within the mentioned pore sites. Red dashed line indicates a contact frequency of 0.5 (50%). *Top panel,* contact frequencies between TMC1 residues and the known blockers; *Middle panel,* contact frequencies between TMC1 residues and the hit compounds from Library 1; *Bottom panel,* contact frequencies between TMC1 residues and the hit drugs from Library 2. TM domains and the respective residues are labeled at the bottom of the figure.

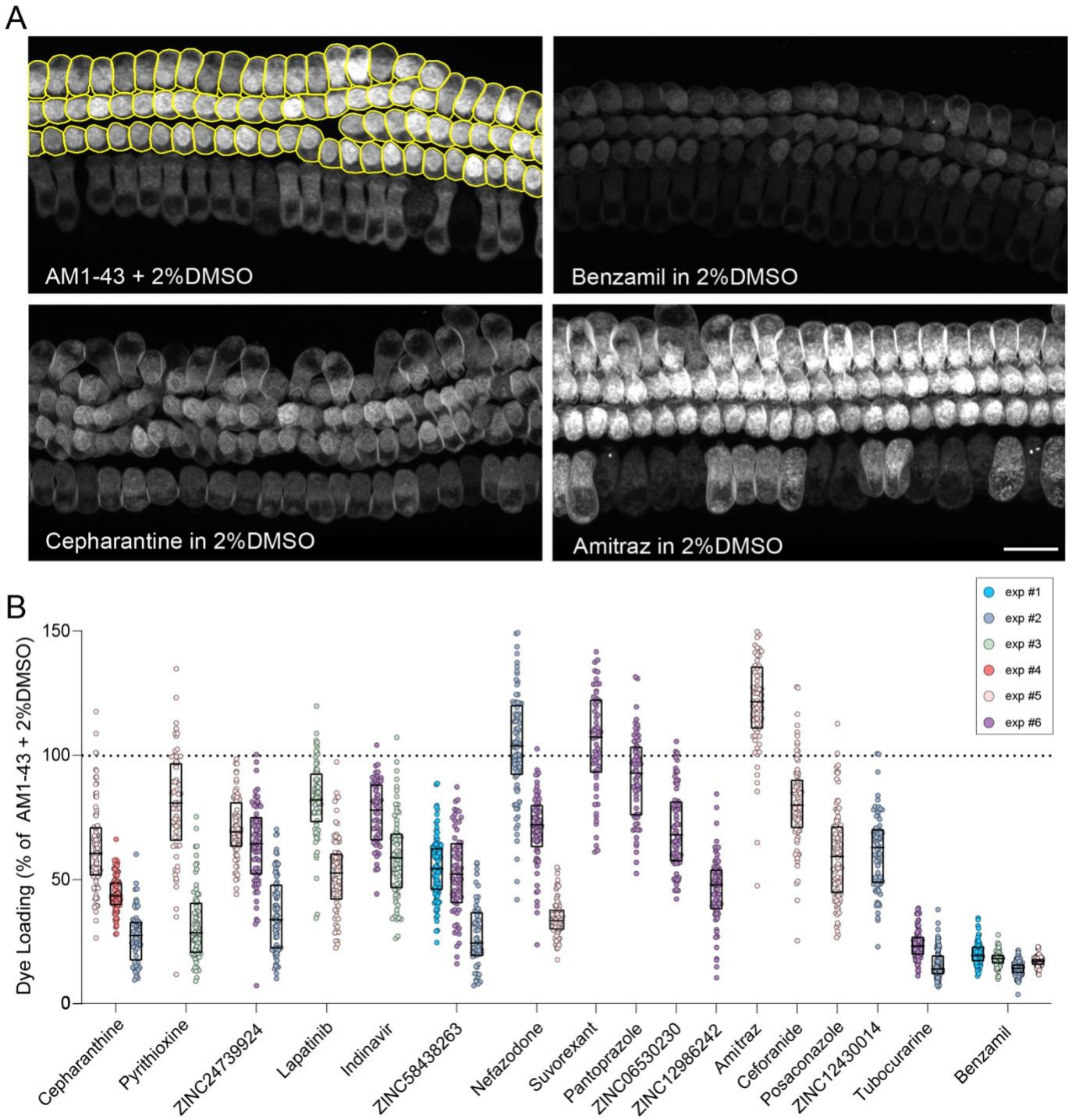

Figure 10. ***Evaluation of predicted TMC1 modulators in live cochlear hair cells using AM1-43 dye uptake assay.*** **(A)** Representative confocal microscopy images of AM1-43 dye loading into hair cells from the middle region of the mouse cochlea (P3+2 days *in vitro*). The *Cellpose* algorithm was used to segment each OHC as individual region of interest (*top left panel*). Dye uptake was reduced by treatment with benzamil (*top right*) and cepharanthine (*bottom left*) but increased following treatment with Amitraz (*bottom right*), when compared to DMSO-treated controls (*top left*). Scale bar, 15 µm. **(B)** Quantification of AM1-43 dye loading into individual OHCs in cochlear explants treated with 16 commercially available hit compounds, normalized to values obtained from corresponding control explants treated with 2% DMSO. The data points are color-coded to match individual experimental sessions. Averages of AM1-43 dye loading intensities across multiple experiments, number of cells analyzed and p-values are reported in *Supp. Figure 5*.

Table 1. Pharmacophore models identified by Phase and scored by PhaseHypoScore[67] (See *Methods*).

Pharmacophore ID	Pharmacophore hypothesis	Number of matching compounds	PhaseHypoScore
ID-1	APRR	7	0.780
ID-2	APR-1	9	0.762
ID-3	APR-2	8	0.759
ID-4	PRR	7	0.698
ID-5	ARR-1	7	0.629
ID-6	ARR-2	9	0.526
ID-7	AHR	7	0.475
ID-8	ARR-3	7	0.418
ID-9	ARR-4	8	0.385
ID-10	HRR	9	0.340

A: Hydrogen-bond acceptor. P: positively charged group. R: aromatic ring. H: hydrophobic group.

Table 2. Re-scoring of docking poses for 15 known blockers using MM-GBSA.

Compound	Without phospholipids ΔG_{bind} (kcal/mol)	With POPC-B and POPC-A ΔG_{bind} (kcal/mol)
E6-berbamine	-73.65	-82.72
FM1-43	-57.69	-84.44
UoS-3607	-54.80	-61.99
Carvedilol derivate 13	-45.35	-53.44
Tubocurarine(*R*)	-44.32	-44.79
Hexamethyleneamiloride	-43.56	-42.01
UoS-962	-41.48	-71.15
UoS-5247	-34.99	-51.17
UoS-3606	-33.38	-40.21
Phenoxybenzamine(R)	-33.26	-36.99
UoS-7692	-31.34	-23.79
Proto-1	-29.81	-37.71
ORC-13661	-27.76	-40.87
Amsacrine	-24.16	-49.74
Benzamil	-20.96	-36.48
Phenoxybenzamine(S)	-19.38	-43.06

Table 3. Structural diversity analysis results for both Library 1 and Library 2 (ΔG_{bind} = kcal/mol) without phospholipids.

Library 1 (non-FDA-approved compounds)			**Library 2 (FDA-approved drugs)**		
Cluster ID	Population (# compounds)	Average ΔG_{bind} ± SD	Cluster ID	Population (# compounds)	Average ΔG_{bind} ± SD
1.1	11 (3)*	-24.74 ± 5.50	2.1	17 (1)*	-34.49 ± 6.46
1.2	7 (3)*	-33.58 ± 10.81	2.2	10 (1)*	-34.46 ± 9.82
1.3	4 (1)*	-31.65 ± 4.81	2.3	6 (1)*	-36.38 ± 6.57
1.4	4 (1)*	-37.62 ± 37.62	2.4	5 (1)*	-21.98 ± 7.57
1.5	3 (1)*	-20.18 ± 2.01	2.5	4 (1)*	-45.88 ± 16.03
1.6	3 (1)*	-39.04 ± 11.70	2.6	3 (1)*	-38.85 ± 14.44
1.7	2	-25.18 ± 4.55	2.7	2 (1)*	-33.68 ± 8.31
1.8	2	-36.65 ± 19.03	2.8	2 (1)*	-25.05 ± 0.54
1.9	2	-21.55 ± 4.99	2.9	1 (1)*	-24.10
1.10	2	-30.21 ± 1.02	2.10	1 (1)*	-20.68
1.11	1	-26.81			
1.12	1	-37.15			
1.13	1	-24.29			
1.14	1	-26.47			
1.15	1	-27.16			
Total = 15	Total = 45 (10)*		Total = 10	Total = 51 (10)*	

*Number of compounds with best ΔG_{bind} suitable for experimental evaluation

Table 4. Re-scoring of the docking energies for the selected hits from Library 1 and Library 2 (ΔG_{bind} = kcal/mol).

Library 1 (non-FDA-approved compounds)			**Library 2 (FDA-approved drugs)**		
Compound	Without phospholipids ΔG_{bind}	With phospholipids ΔG_{bind}	Compound	Without phospholipids ΔG_{bind}	With phospholipids ΔG_{bind}
ZINC58438263	-52.49	-70.02	**Posaconazole**	-59.84	-104.39
ZINC12986242	-46.71	-59.54	**Cepharanthine**	-53.79	-40.41
ZINC06530230	-44.86	-50.16	**Indinavir**	-53.76	-58.04
ZINC07001403	-42.20	-70.48	**Nefazodone**	-46.31	-66.65
ZINC12756822	-40.36	-67.09	**Lapatinib**	-45.73	-19.26
ZINC12430014	-38.22	-77.04	**Suvorexant**	-39.55	-39.03
ZINC33126270	-35.82	-47.73	**Pantoprazole**	-30.72	-42.62
ZINC12890205	-32.04	-36.62	**Pyritinol**	-25.42	-37.32
ZINC64590918	-28.47	-51.42	**Amitraz**	-24.10	-30.02
ZINC24739924	-22.42	-39.93	**Ceforanide**	-20.68	-23.29

Compounds in bold were evaluated experimentally, upon commercial availability.

SUPPLEMENTARY MATERIAL

Identification of Druggable Binding Sites and Small Molecules as Modulators of TMC1

Pedro De-la-Torre[1,*,†], Claudia Martínez-García[2,†], Paul Gratias[1,†], Matthew Mun[1], Paula Santana[3], Nurunisa Akyuz[4], Wendy González[5], Artur A. Indzhykulian[1,*], David Ramírez[2,*].

Affiliations:

[1]Department of Otolaryngology - Head and Neck Surgery, Harvard Medical School and Mass Eye and Ear, Boston, MA, USA

[2]Department of Pharmacology, Faculty of Biological Sciences, University of Concepción, Chile.

[3]Facultad de Ingeniería, Instituto de Ciencias Químicas Aplicadas, Universidad Autónoma de Chile, Santiago, Chile

[4]Department of Neurobiology, Harvard Medical School, Boston, MA, USA

[5]Center for Bioinformatics and Molecular Simulations (CBSM), University of Talca, Talca 3460000, Chile

[*]Correspondence should be addressed to:

dramirezs@udec.cl,

inartur@hms.harvard.edu,

pedro_delatorremarquez@meei.harvard.edu

[†]These authors contributed equally to this work

Supplementary Table 1. Known MET channel blockers used to build a common pharmacophore model (related to *Figure 1*)

ID	Compound	Concentration reported	MET channel	Reference
1	UoS-7692	50 µM	80% block	(Kenyon et al., 2021)
2	UoS-3607	50 µM	70% block	(Kenyon et al., 2021)
3	UoS-3606	50 µM	80% block	(Kenyon et al., 2021)
4	UoS-5247*	50 µM	20% block (Steep release)	(Kenyon et al., 2021)
5	UoS-962	50 µM	20% block	(Kenyon et al., 2021)
6	Proto-1	10 µM	80% control hair cells	(Owens et al., 2008)
7	E6 berbamine	25 µM	Significant hair cells damage	(Kruger et al., 2016)
8	Hexamethyleneamiloride	10 µM	50% control hair cells survival	(Ou et al., 2009)
9	Amsacrine	10 µM	50% control hair cells survival	(Ou et al., 2009)
10	Phenoxybenzamine	10 µM	39% control hair cells survival	(Ou et al., 2009; Majumder et al., 2017)
11	Carvedilol derivate 13	5 µM	50% block	(O'Reilly et al., 2019)
12	ORC-13661	8.3 µM	85% control hair cells	(Kitcher et al., 2019; Sarwat Chowdhury, et al., 2018)
13	FM1-43	20 µM	95% block	(Gale et al., 2001, Jason R Meyers et al., 2003)

***** UoS-5247 has been reported as a week MET blocker (Kenyon et al., 2021). We included this compound to introduce structural diversity due its lipophilic substituent (See also *Figure 1*)

Supplementary Table 2. Matching compounds for each pharmacophore. Compounds that match the pharmacophore are marked with an X. Hydrogen bond acceptor (A), positively charged group (P), aromatic ring (R), and hydrophobic group (H).

Compound	APRR	APR-1	APR-2	PRR	ARR-1	ARR-2	AHR	ARR-3	ARR-4	HRR	Total matches
UoS-7692	X	X	X	X	X	X	X		X	X	9
UoS-3607	X	X	X	X	X	X	X	X	X		9
UoS-3606					X		X				2
UoS-5247 *											0
UoS-962	X	X	X	X	X	X			X	X	8
Proto-1						X		X	X	X	4
E6 bermamine	**X**	**X**	**X**	**X**	**X**	**X**	**X**	**X**	**X**	**X**	**10**
Hexamethyleneamiloride		X					X				2
Amsacrine	X	X	X	X		X		X		X	7
Phenoxybenzamine	**X**	**X**	**X**	**X**	**X**	**X**	**X**	**X**	**X**	**X**	**10**
Carvedilol derivate 13	**X**	**X**	**X**	**X**	**X**	**X**	**X**	**X**	**X**	**X**	**10**
ORC-13661		X	X			X		X	X	X	6
FM1-43										X	1
Total	7	9	8	7	7	9	7	7	8	9	

***** UoS-5247 is a weak MET blocker previously reported to have a steep release activity (Kenyon et al., 2021). It was selected to increase structural diversity due its lipophilic substituent. However, upon Phase analysis, UoS-5247 did not fit to any of the ten pharmacophores used in this study, suggesting that the lipophilic substituent and the absence of a bigger aromatic moiety, such as benzimidazole (also present in UoS-7692, UoS-3607, UoS-3606), could be detrimental to the interaction with the MET channel (Kenyon et al., 2021).

Supplementary Table 3. Matrix constructed with the PhaseScreenScore that each compound of the non-FDA-approved Library 1 obtained for each pharmacophore after 2nd-step PBVS with Phase. The top-5 hits (according to the *TPS*$_s$, as well as the last 5 solutions are presented

N°	Compound	APRR	APR-1	APR-2	PRR	ARR-1	ARR-2	AHR	ARR-3	ARR-4	HRR	
1	ZINC26876007	2.449	2.272	2.290	2.438	2.103	2.208	2.080	1.708	2.054	1.910	21.512
2	ZINC93401109	2.045	2.298	2.357	2.309	1.994	2.203	1.700	1.778	2.165	2.152	21.001
3	ZINC51125638	2.172	2.307	2.081	2.323	1.998	2.209	1.958	2.043	1.945	1.884	20.920
4	ZINC91304884	2.439	2.407	2.287	2.378	2.150	2.317	1.668	1.676	1.895	1.700	20.917
5	ZINC60557463	2.094	2.274	2.241	2.243	2.015	2.341	1.653	1.755	2.111	2.065	20.792
…	…	…	…	…	…	…	…	…	…	…	…	…
4183	ZINC39970059	0	0	0	0	1,506	0	0	0	0	0	1,506
4184	ZINC39967993	0	0	0	0	1,337	0	0	0	0	0	1,337
4185	ZINC63373196	0	0	0	0	1,309	0	0	0	0	0	1,309
4186	ZINC39708296	0	0	0	0	1,245	0	0	0	0	0	1,245
4187	ZINC39969398	0	0	0	0	0	0	1.157	0	0	0	1.157

A: hydrogen-bond acceptor. **P**: positively charged group. **R**: aromatic ring. **H**: hydrophobic group. ***TPS$_S$***: Total-PhaseScreenScore

Supplementary Table 4. Matrix built with the PhaseScreenScore that each compound of the FDA-approved drug (Library 2) obtained for each pharmacophore after 2nd-step PBVS with Phase. The top-5 hits (according to the , as well as the last 5 solutions are presented.

N°	Compound	APRR	APR-1	APR-2	PRR	ARR-1	ARR-2	AHR	ARR-3	ARR-4	HRR	
1	Carvedilol	1.736	2.301	1.762	1.666	2.298	2.168	1.651	1.544	1.825	1.642	18.593
2	Candesartan Cilexetil	1.498	1.609	1.465	1.776	1.981	1.923	1.912	1.809	2.079	1.698	17.750
3	Olmesartan Medoxomil	1.532	1.511	1.508	1.557	2.212	1.999	1.719	1.886	1.968	1.767	17.659
4	Candesartan	1.602	1.709	1.532	1.759	1.821	2.041	1.964	1.599	1.895	1.551	17.473
5	Amitraz	1.836	2.200	1.297	1.924	1.513	1.867	1.985	1.486	1.822	1.484	17.414
…	…	…	…	…	…	…	…	…	…	…	…	…
902	Nortrupityline	0	0	0	0	0	0,636	0	0	0	0	0,636
903	Estradiol Cypionate	0,62	0	0	0	0	0	0	0	0	0	0,620
904	Valganciclovir	0	0,547	0	0	0	0	0	0	0	0	0,547
905	Cefcapene Pivoxil	0,506	0	0	0	0	0	0	0	0	0	0,506
906	Trimeprazine	0	0	0	0	0	0	0.419	0	0	0	0.419

A: hydrogen-bond acceptor**. P:** positively charged group**. R:** aromatic ring**. H:** hydrophobic group**.** : Total-PhaseScreenScore

Supplementary Table 5. List of key residues located in the top, middle, and bottom binding sites of TMC1 involved in binding of small molecules (related to colored regions in *Figure 5* and *Figure 6*)

Sites	Residues
Top	N404, M407, F451, E458, E520, R523, L524, S527, M583, POPC-B
Middle	S408, **G411**, **M412**, L443, L444, **N447**, L448, **D528**, T531, **T532**, I536, F579, N580, G582, R601
Bottom	Y182, P415, T416, D419, L436, L437, I440, T535, D540, R543, T566, E567, F568, **D569**, S571, **G572**, N573, L575, A576, L577, Q609, A612, V613, N617, POPC-A
Zwitterionic-like network ZN1*	D239, N404, E458, E520, R523, POPC-B
Zwitterionic-like network ZN2	**D528**, T531, **T532**, N580, N598, R601
Zwitterionic-like network ZN3*	T416, D419, E423, T535, D540, R543, D569, N573, E620, R622

*The polar head of POPC-A points towards the bottom site forming a zwitterionic-like interaction network with R543, D569, E567, E620, and R622, key for both ligand and phospholipid binding. Additionally, the polar head of POPC-B forms a similar zwitterionic-like network with R523, N401, and N404. residues Hydrophobic tails of both phospholipids form a sidewall between TM4 and TM6 (see **Supp. Fig 3**). Residues in bold are known deafness mutation sites or known to alter TMC1 leak courrents[1].

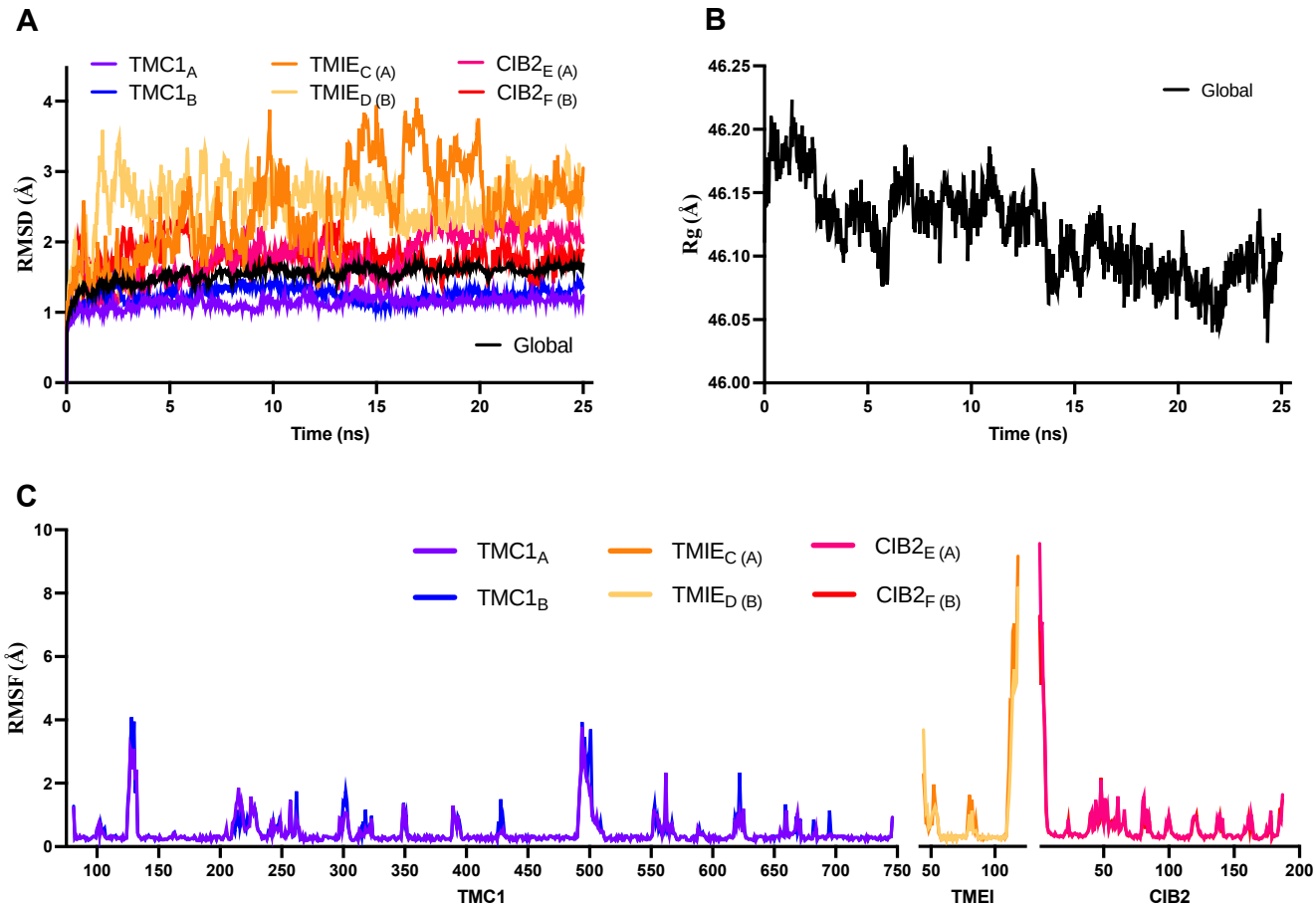

Supplementary Figure 1. Molecular dynamics simulations of MET complex. (A) Time dependence of the Root Mean Squared Deviation (RMSD) for TMC1, TMIE and CIB2 backbones during the 25ns MDs. **(B)** Radius of gyration (Rg) to study the compactness of the protein. **(C)** Root Mean Squared Fluctuation (RMSF) characterizing the internal residue fluctuation of TMC1, TMIE and CIB2 during the 25ns MDs.

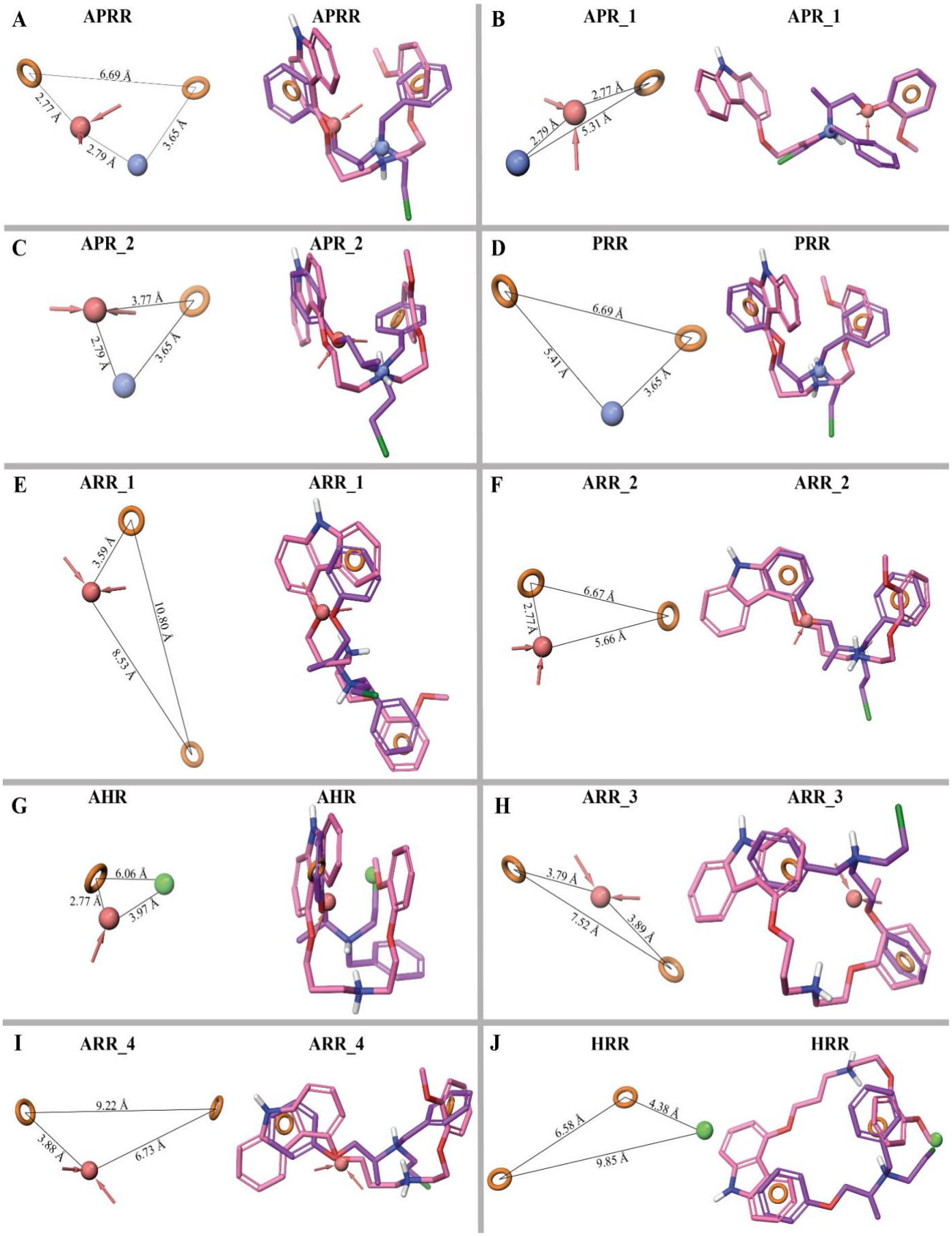

Supplementary Figure 2. 3D view of the 10 common pharmacophores of 13 known MET channel blockers. (A-K) Pharmacophore models of MET channel blockers (Figure 1). Hydrogen-bond acceptor features (*A*) in red, aromatic rings (*R*) in orange circles, positively charged group (*P*) in blue, and hydrophobic group (H) in green beads. Distances between the vector features are labeled. Superposed structures of the MET blockers phenoxybenzamine (purple) and carvedilol derivative 13 (pink) with the vector features of each pharmacophore. These two compounds fit to all the 10 pharmacophores reported in Table 1 (See Supp Table 2). 3D structures were depicted with Pymol[2]

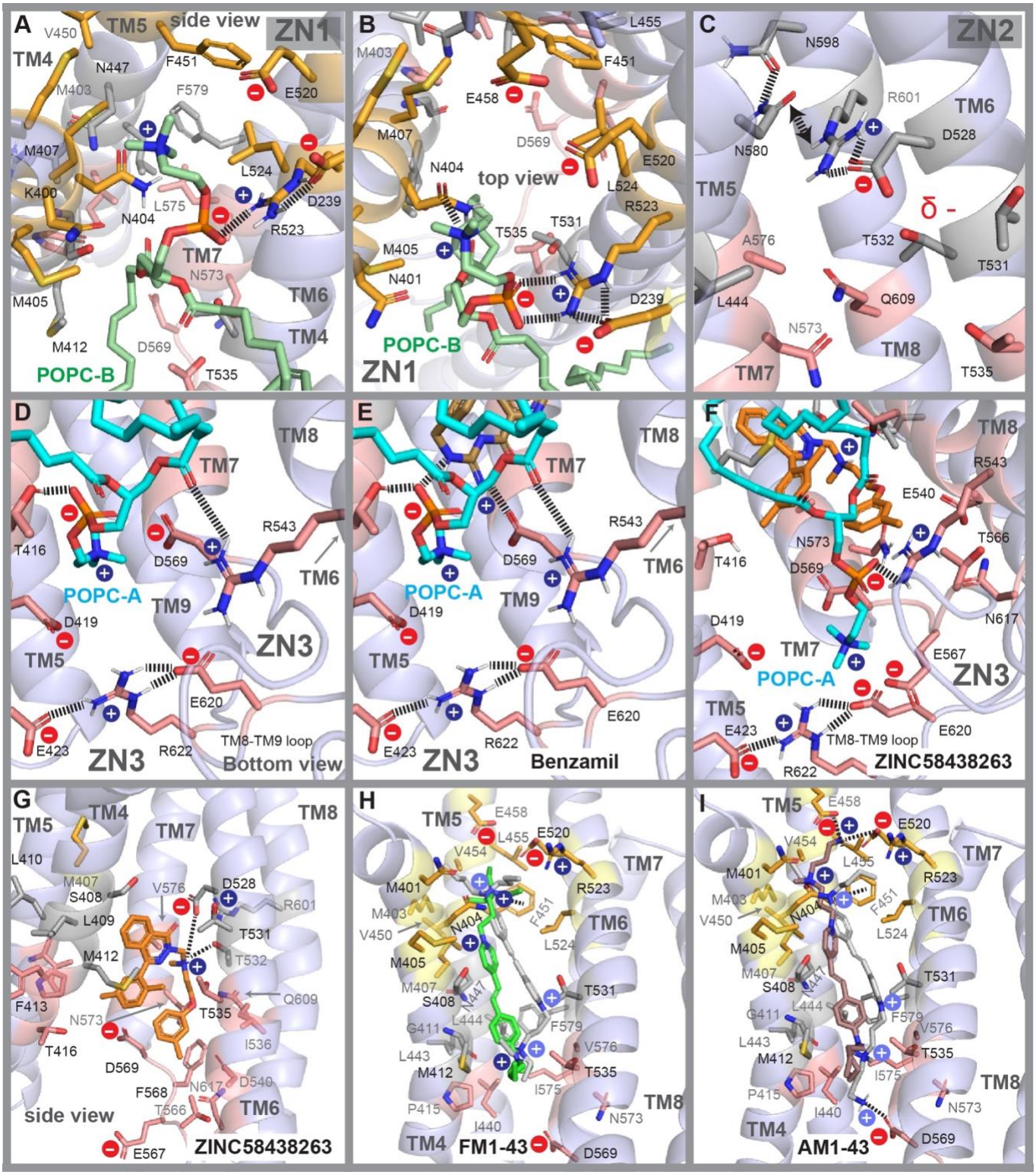

Supplementary Figure 3. Zwitterionic sites and binding modes of ZINC58438263, FM1-43 and AM143 in the TMC1 pore. (A-B) Side and top views of the ZN1 site showing POPC-B (lime). Dashed lines represent interactions between the negative head of the phospholipid with R523 and D239. The positive charged iminium group is placed near N404 forming salt bridges. (C) Side view of the ZN2 site. TM4 was removed for clarity. The amino acids N580, N598, R601, and D528 closely interact forming hydrogen bond and salt bridge interactions, stabilizing TM5, TM6, and TM8 at the middle site of the pore. The residues D528, T531, and T532 form an electronegatively charged area (δ^-) involving in ligand binding. (D-E) Bottom view of the ZN3 site in absence and presence of benzamil. Benzamil displays key interactions with D569 and the negative head of POPC-A, which in turn interact with T416 forming hydrogen bond interactions with TM4. Similarly, the carbonyl group of POPC-A interacts with R543 located in TM6. The ZN3 site might be relevant for phospholipid and ligand stabilization at the bottom site. Furthermore, other stabilizing interactions are displayed between R622 and the charged residues E423 and E620 which clamp TM4, TM8, and TM9 with salt-bridge interactions, stabilizing the bottom cavity. (F) Bottom view of the ZN3 site and binding of ZINC58438263 along with POPC-A. ZINC58438263 does not displays direct interactions with D569 as benzamil. Interactions between R622, E423, and E620 are also showed as in panel C-E. (G) Side view of the binding mode of ZINC58438263, displaying direct interactions between the iminium group and both D528 and T532. Neighboring residues are showed, specially M412 forming van der Waals interactions. (H) Two binding docking conformations predicted for FM1-43. The first binding mode

conformation of FM1-43 (green) shows its triethylammonium charged group forming a cation-π stacking interaction with F451 at the top site near ZN1. The second binding mode (in gray) is inverted pointing the triethylammonium charged group towards the bottom site near M412 and T535. In this scenario, the positively charged dibutylamine group of FM1-43 is not placed near F451 as analyzed above. (I) Side view of the binding mode of AM1-43 (brown). This first binding mode conformation shows similar interactions to those displayed by FM1-43 (panel H, green), with the difference that the elongated and protonated butylamine group forms interactions with E458 and E520 at the ZN1 site near the entry of the pore. The second binding mode of AM1-43 (gray) is inverted with the same group now forming a direct salt bridge with D569 at the bottom site. In this second scenario, the positively charged dibutylamine group, mimics the same cation-π stacking interaction with F451 displayed by the triethylammonium charged group of FM1-43, as in panel H.

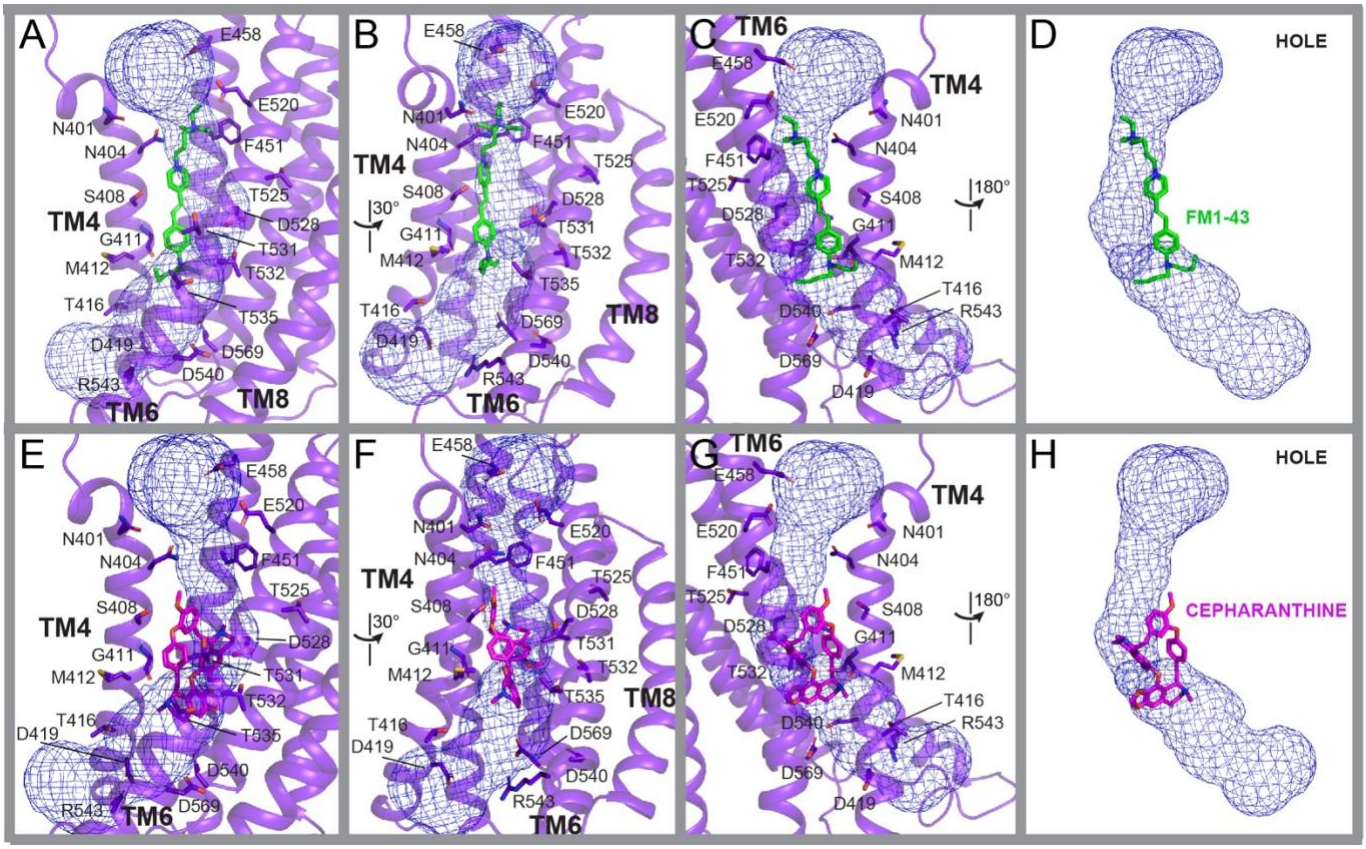

Supplementary Figure 4. Structural features of TMC1 pore with HOLE including ligands. (A-D) Structural representation of the pore and FM1-43. **(A)** Side view of a TMC1 protomer showing a curved pore calculated by HOLE[3] in blue mesh representation. Docking pose of FM1-43 is showed in green licorice representation (as in Figure 5 and 6). **(B-C)** 30° and 180° rotation view from panel *a*, respectively. **(B)** View of the mesh contour and FM1-43 as in panel *c***.** As predicted by docking, some areas of the FM1-43 molecule are outside of the mesh contour predicted by HOLE, suggesting that some ligand binding-residues are different than those used by HOLE to calculate the mesh-pore contour. **(E-H)** Structural representation of the pore and the docked cepharanthine, as showed in panels *a-d*. Similar to FM1-43, a portion of the cepharanthine molecule is docked inside the mesh contour predicted by HOLE, while two aromatic moieties are placed outside the mesh contour. In both cases, the positively charged nitrogen atoms of FM1-43 and cepharanthine are located inside the mesh contour of the pore. Results suggest that both elongated and spherical ligands bind to the TMC1 pore occupying regions not predicted by HOLE.

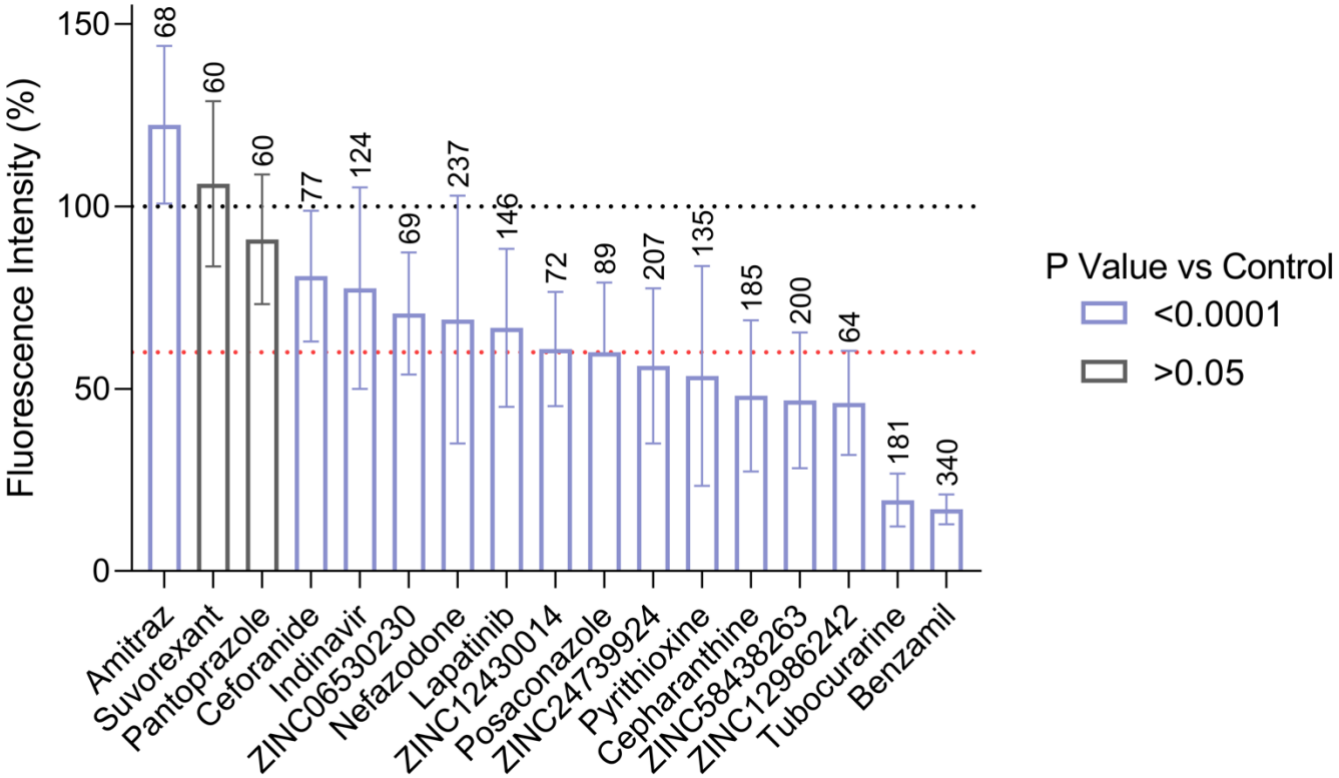

Supplementary Figure 5. Pooled average intensity values of AM1-43 dye uptake across all experiments for each compound tested. Data presented as Mean ± S.D. with the color of the bars representing the p-value vs. control (one-way ANOVA), the number of cells quantified per experiment are listed above each bar. Black and red dashed lines represent the control (100%) and the effective blockage (60%) thresholds, respectively.

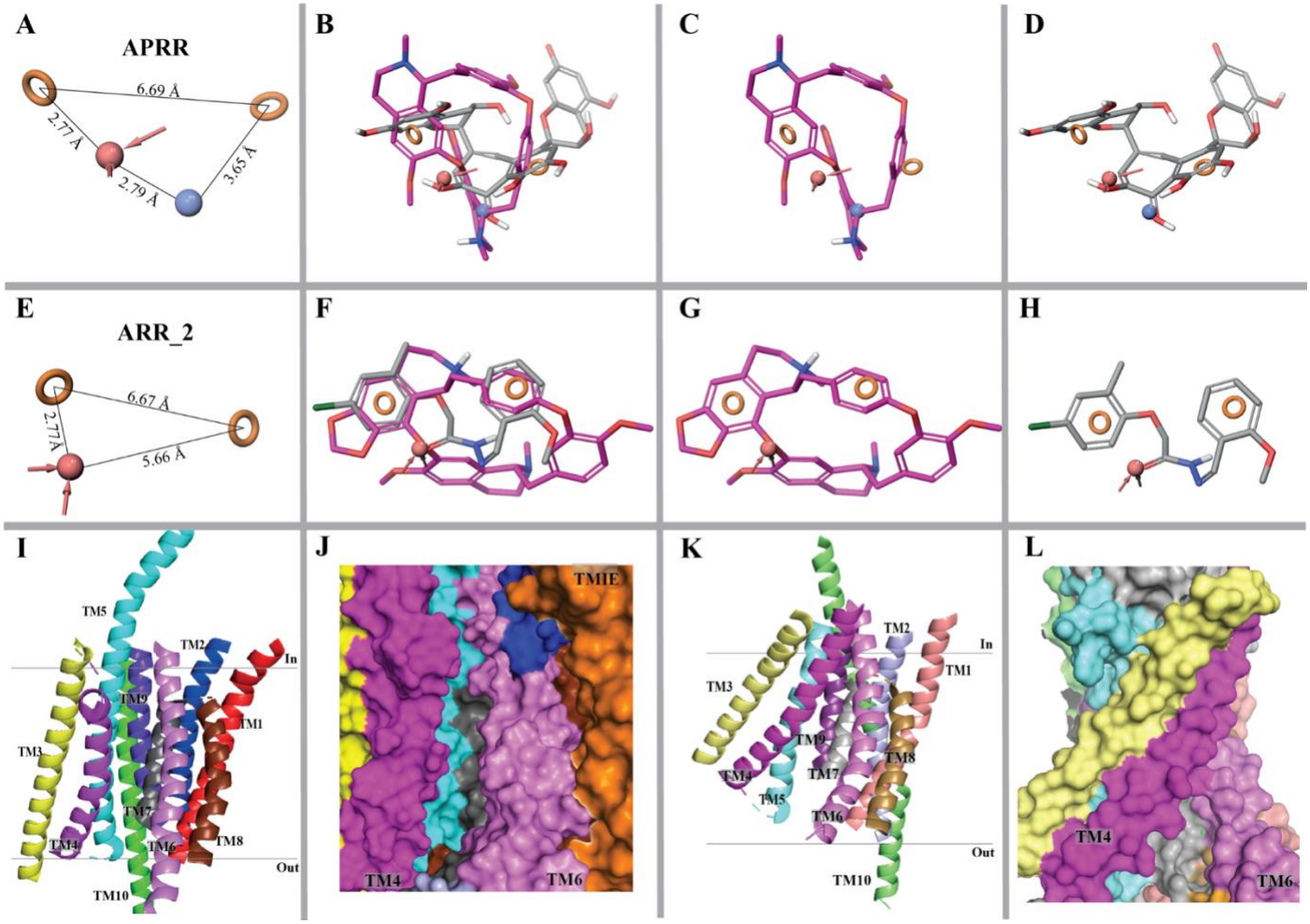

Supplementary Figure 6. 3D view of the 2 common pharmacophores of TMC1 and TMEM16 channel blockers. **(A** and **E)** Pharmacophore models of MET channel blockers (Figure 1), ID1 and ID6, respectively (Table1). **(A)** APRR pharmacophore model. Hydrogen-bond acceptor features (*A*) in red, aromatic rings (*R*) in orange circles and positively charged group (*P*) in blue beads. Distances between the vector features are labeled. **(B)** Superposed structures of the hit compound cepharanthine (magenta) and the theaflavin with a protonated carbonyl group (gray) with the vector features of the TMC1-pharmacophore APRR. **(C-D)** Structural alignment of cepharanthine and theaflavin with the APRR vector features, respectively. **(E)** ARR_2 pharmacophore model. **(F)** Superposed structures of the hit compound cepharanthine (magenta) and Ani9 (gray) with the vector features of the TMC1-pharmacophore ARR-2. **(G-H)** Structural alignment of cepharanthine and Ani9 with the ARR-2 vector features, respectively. Theaflavin and Ani9 are inhibitors of TMEM16A[4]. **(I)** Cartoon representation of an open-like conformation of TMC1. Loops are removed for clarify and TM domains are colored and labeled for clarity. TM4 is colored in magenta and TM6 is colored in dark pink as a reference, showing a parallel (I I) conformation. **(J)** Surface representation of TMC1 protomer as in Figure 5. TM4 and TM6 are colored as in panel I, showing the parallel conformation. Other TM domains are colored as in panel I, along with TMIE as a reference (dark orange). (K) Cartoon representation of TMEM16A as in panel I. TM4 is colored in light magenta and TM6 in light pink, both showing an inverted V conformation clashing at the upper-top site. (L) Surface representation of TMEM16A. View and colors as in panel J. TM4 (light magenta) and TM6 (light pink) forms a V conformation that closes the pore at the upper-top site. A space cavity (cyan, gray, and light brown) is shown at the bottom between the separated TM4 and TM6 domains.

References in supplementary data

1. Liu, S. *et al.* TMC1 is an essential component of a leak channel that modulates tonotopy and excitability of auditory hair cells in mice. *eLife* **8**, e47441 (2019).
2. DeLano, W. L. Pymol. (2002).
3. Smart, O. S., Neduvelil, J. G., Wang, X., Wallace, B. A. & Sansom, M. S. HOLE: a program for the analysis of the pore dimensions of ion channel structural models. *J. Mol. Graph.* **14**, 354–60, 376 (1996).
4. Al-Hosni, R., Ilkan, Z., Agostinelli, E. & Tammaro, P. The pharmacology of the TMEM16A channel: therapeutic opportunities. *Trends Pharmacol. Sci.* **43**, 712–725 (2022).